ATLAS CONF Note

ATLAS-CONF-2019-011

March 27, 2019

Search for bottom-squark pair production with the ATLAS detector in final states containing Higgs bosons, b-jets and missing transverse momentum

The ATLAS Collaboration

The result of a search for the pair production of the supersymmetric partner of the bottom-quark ($\tilde{b}_1$) using 139 fb^{-1} of data collected at $\sqrt{s}$ = 13 TeV by the ATLAS detector in Run 2 is reported. In the supersymmetric scenarios considered, each of the bottom-squarks decay to a b-quark and the second lightest neutralino, $\tilde{b}_1 \rightarrow b + \tilde{\chi}_2^0$. Each $\tilde{\chi}_2^0$ is assumed to subsequently decay with 100% branching ratio to the Standard-Model-like Higgs boson (h) and the lightest neutralino: $\tilde{\chi}_2^0 \rightarrow h + \tilde{\chi}_1^0$. The $\tilde{\chi}_1^0$ is assumed to be the lightest supersymmetric particle (LSP) and is stable. Two signal mass configurations are targeted: the first has a constant LSP mass of 60 GeV; and the second has a constant mass difference between the $\tilde{\chi}_2^0$ and $\tilde{\chi}_1^0$ of 130 GeV. The final states considered contain no charged leptons, three or more b-jets, and large missing transverse momentum. No significant excess of events over the Standard Model background expectation is observed in any of the signal regions considered. Limits at the 95% confidence level are placed in the supersymmetric models considered, and bottom-squarks with mass up to 1.45 TeV are excluded.

ATLAS-CONF-2019-011
29 March 2019

1 Introduction

Supersymmetry (SUSY) [1–6] provides an extension of the Standard Model (SM) that solves the hierarchy problem [7–10] by introducing partners of the known bosons and fermions. In R-parity-conserving models [11], SUSY particles are produced in pairs and the lightest supersymmetric particle (LSP) is stable and provides a candidate for dark matter [12, 13]. The superpartners of the SM bosons (the Wino, Bino and Higgsinos) mix to form the observed neutralinos ($\tilde{\chi}^0_{1,2,3,4}$) and charginos ($\tilde{\chi}^\pm_{1,2}$). For a large selection of models, the LSP is the lightest neutralino ($\tilde{\chi}^0_1$). Naturalness considerations suggest that the supersymmetric partners of the third-generation quarks are light [14, 15]. Under this assumption, the lightest bottom-squark ($\tilde{b}_1$) and lightest top squark ($\tilde{t}_1$) mass eigenstates[1] could be significantly lighter than the other squarks and the gluinos. As a consequence, $\tilde{b}_1$ and $\tilde{t}_1$ could be pair-produced with relatively large cross-sections at the Large Hadron Collider (LHC). Depending on the mass hierarchy considered, it is possible that the $\tilde{b}_1$ and $\tilde{t}_1$ could decay with Higgs bosons in the final state, allowing the Higgs boson to be used as a probe for new physics.

This paper presents a search for the pair production of bottom-squarks decaying to the LSP via a complex decay chain containing the second lightest neutralino ($\tilde{\chi}^0_2$), and the SM-like Higgs boson (h): $\tilde{b}_1 \rightarrow b + \tilde{\chi}^0_2$ and subsequently $\tilde{\chi}^0_2 \rightarrow h + \tilde{\chi}^0_1$. Such a decay hierarchy is predicted in minimal supersymmetric extension of the SM (MSSM) [16, 17] models, with h taken to be the lightest of the neutral bosons introduced in the MSSM. When the LSP is bino-like and the $\tilde{\chi}^0_2$ is a wino-higgsino mixture, the branching ratio (B) of $\tilde{\chi}^0_2 \rightarrow h + \tilde{\chi}^0_1$ is enhanced with respect to the other possible $\tilde{\chi}^0_2$ decays. The Higgs boson mass is taken to be 125 GeV. The decay into a pair of b-quarks is assumed to be SM-like (B = 58% [18]), although it could be enhanced or reduced in the MSSM.

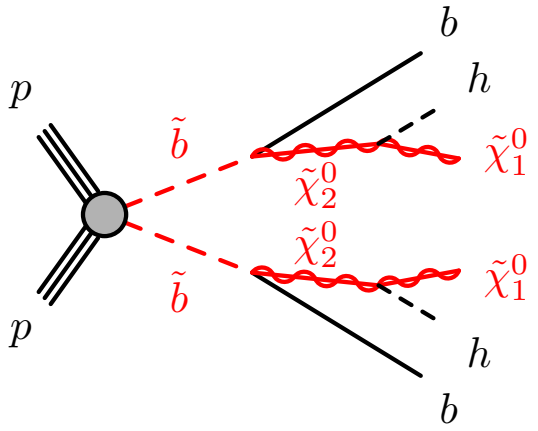

Figure 1: Graphical representation of the SUSY signal targeted by this analysis. Bottom-squarks are produced in pairs and subsequently decay to $b\tilde{\chi}^0_2$ with B = 100%. The two $\tilde{\chi}^0_2$ particles decay to $h\tilde{\chi}^0_1$ also with B = 100%.

This search is interpreted within simplified model scenarios [19, 20] and Figure 1 illustrates the targeted model. In the first set of models, already considered in Run 1 by the ATLAS collaboration [21], the mass of the $\tilde{\chi}^0_1$ is fixed at 60 GeV. The bottom-squark and $\tilde{\chi}^0_2$ masses vary in the ranges 250–1600 GeV and 200–1500 GeV, respectively. The assumption on the $\tilde{\chi}^0_1$ mass is motivated by dark matter relic density measurements and might be favoured in Higgs-pole annihilation scenarios [22] where $m_{\tilde{\chi}^0_1} \simeq m_h/2$. The

[1] The scalar partners of the left-handed and right-handed chiral components of the bottom quark ($\tilde{b}_{L,R}$) or top quark ($\tilde{t}_{L,R}$) mix to form mass eigenstates for which $\tilde{b}_1$ and $\tilde{t}_1$ are defined as the lighter of the two states.

previous search performed by ATLAS using the Run 1 LHC dataset excluded bottom-squark masses up to 750 GeV in this scenario [21].

The second set of SUSY models assumes a fixed mass difference between the $\tilde{\chi}_2^0$ and $\tilde{\chi}_1^0$, sufficient to produce an on-shell Higgs boson. The mass difference, $\Delta m(\tilde{\chi}_2^0, \tilde{\chi}_1^0)$, is set to 130 GeV, whilst bottom-squark and $\tilde{\chi}_1^0$ masses vary in the ranges 400 to 1500 GeV and 1 to 800 GeV, respectively. A similar scenario has been considered by the CMS collaboration in Ref. [23], where the $h \to \gamma\gamma$ decay mode was exploited. Bottom-squark masses up to 450 GeV have been excluded. No prior ATLAS searches have been performed targeting these models.

The final states are characterised by a unique signature which contains many jets, up to six that can be identified as originating from the fragmentation of b-quarks (referred to as b-jets), missing transverse momentum ($\mathbf{p}_{\mathrm{T}}^{\mathrm{miss}}$, the magnitude thereof referred to as $E_{\mathrm{T}}^{\mathrm{miss}}$), and zero charged leptons (referred to as leptons). New selections and dedicated procedures aiming to maximize the efficiency of reconstructing the Higgs boson candidates decaying into a b-quark-pair are employed in this article. Section 2 presents a brief overview of the ATLAS detector, with Section 3 describing the data and simulated samples used in the analysis. The event reconstruction methods are explained in Section 4. An overview of the analysis strategy is presented in Section 5, with the background estimation strategy discussed in Section 6. The systematic uncertainties considered in the analysis are described in Section 7. Section 8 presents the results and interpretation thereof, with the conclusions presented in Section 9.

2 ATLAS detector

The ATLAS detector [24] is a multi-purpose particle physics detector with a forward-backward symmetric cylindrical geometry and nearly 4π coverage in solid angle.[2] The inner tracking detector consists of pixel and silicon microstrip detectors covering the pseudorapidity region $|\eta| < 2.5$, surrounded by a transition radiation tracker which enhances electron identification in the region $|\eta| < 2.0$. Between Run 1 and Run 2, a new inner pixel layer, the insertable B-layer [25], was added at a mean sensor radius of 3.3 cm. The inner detector is surrounded by a thin superconducting solenoid providing an axial 2 T magnetic field and by a fine-granularity lead/liquid-argon (LAr) electromagnetic calorimeter covering $|\eta| < 3.2$. A steel/scintillator-tile calorimeter provides hadronic coverage in the central pseudorapidity range ($|\eta| < 1.7$). The endcap and forward regions ($1.5 < |\eta| < 4.9$) of the hadronic calorimeter are made of LAr active layers with either copper or tungsten as the absorber material. An extensive muon spectrometer with an air-core toroidal magnet system surrounds the calorimeters. Three layers of high-precision tracking chambers provide coverage in the range $|\eta| < 2.7$, while dedicated fast chambers allow triggering in the region $|\eta| < 2.4$. The ATLAS trigger system consists of a hardware-based level-1 trigger followed by a software-based high-level trigger [26].

[2] ATLAS uses a right-handed coordinate system with its origin at the nominal interaction point in the centre of the detector. The positive x-axis is defined by the direction from the interaction point to the centre of the LHC ring, with the positive y-axis pointing upwards, while the beam direction defines the z-axis. Cylindrical coordinates (r, ϕ) are used in the transverse plane, ϕ being the azimuthal angle around the z-axis. The component of momentum in the transverse plane is denoted by p_{T}. The pseudorapidity η is defined in terms of the polar angle θ by $\eta = -\ln\tan(\theta/2)$. Rapidity is defined as $y = 0.5\ln[(E + p_z)/(E - p_z)]$ where E denotes the energy, and p_z is the component of the momentum along the beam direction. The separation in η, ϕ space of two objects is given by $\Delta R = \sqrt{(\Delta\eta)^2 + (\Delta\phi)^2}$.

3 Data and simulated event samples

The dataset used corresponds to a total of 139 fb^{-1} of proton-proton (pp) collision data collected by the ATLAS detector with a centre-of-mass energy of 13 TeV and a 25 ns proton bunch crossing interval in the period between 2015 and 2018. All detector subsystems were required to be operational during data taking. The average number of interactions per bunch crossing (pileup) increased from $\langle\mu\rangle = 20$ (2015–2016 dataset) to $\langle\mu\rangle = 37$ (2018 dataset), with a highest $\langle\mu\rangle = 38$ (2017 dataset). The uncertainty in the combined 2015–2018 integrated luminosity is 1.7%. It is derived following a methodology similar to that detailed in Ref. [27], and using the LUCID-2 detector for the baseline luminosity measurements [28], from calibration of the luminosity scale using x–y beam-separation scans.

Events used in this analysis are required to pass an $E_{\text{T}}^{\text{miss}}$ trigger [29]. This trigger is fully efficient for events with reconstructed $E_{\text{T}}^{\text{miss}} > 250$ GeV. Additional single-lepton triggers requiring electrons or muons are used to estimate the SM backgrounds, with an offline selection of $p_{\text{T}}(\ell) > 27$ GeV used to ensure the trigger is fully efficient.

Dedicated Monte-Carlo (MC) simulated samples are used to model SM processes and estimate the expected signal yields. All samples are produced using the ATLAS simulation infrastructure [30] and GEANT4 [31], or a faster simulation based on a parameterisation of the calorimeter response and GEANT4 for the other detector systems.

SUSY signal samples are generated with MadGraph v2.6.2 [32] at leading order (LO) and interfaced to PYTHIA v8.230 [33] with the A14 [34] set of tuned parameters (tune) for the modelling of the parton showering (PS), hadronisation and the underlying event. The matrix element (ME) calculation is performed at tree level and includes the emission of up to two additional partons. The ME–PS matching is done using the CKKW-L [35] prescription, with a matching scale set to one quarter of the bottom-squark mass. The NNPDF23LO [36] parton distribution function (PDF) set is used. Signal cross sections are calculated to approximate next-to-next-to-leading order in the strong coupling constant, adding the resummation of soft gluon emission at next-to-next-to-leading-logarithmic accuracy (approximate NNLO+NNLL) [37–40]. The nominal cross section and the uncertainty are derived using the PDF4LHC15_mc PDF set, following the recommendations of Ref. [41].

The SM backgrounds considered in this analysis are: $t\bar{t}$ pair production; single-top production; Z+jets; W+jets; $t\bar{t}$ production with an electroweak (ttV) or Higgs (ttH) boson; and diboson production. The samples are simulated using different MC generator programs depending on the process. Pair production of top quarks, $t\bar{t}$, is generated using POWHEG v2 [42] interfaced with PYTHIA v8.230 and the A14 tune with the NNPDF23LO PDF set for the ME calculations. The h_{damp} parameter in POWHEG, which controls the p_{T} of the first additional emission beyond the Born level and thus regulates the p_{T} of the recoil emission against the $t\bar{t}$ system, is set to 1.5 times the top-quark mass ($m_t = 172.5$ GeV) as a result of studies documented in Ref. [43]. The generation of single top quarks in the Wt-channel, s-channel and t-channel production modes is performed by POWHEG v2 similarly to the $t\bar{t}$ samples. For all processes involving top quarks, top quark spin correlations are preserved. All events with at least one leptonically decaying W boson are retained. Fully hadronic $t\bar{t}$ and single-top events do not contain sufficient $E_{\text{T}}^{\text{miss}}$ to contribute significantly to the background. The production of $t\bar{t}$ pairs in association with electroweak vector bosons (W, Z) or Higgs bosons is modeled by samples generated at NLO using MadGraph v2.2.3 and showered with PYTHIA v8.212. Events containing W or Z bosons with associated jets, including jets from the fragmentation of b- and c-quarks, are simulated using the SHERPA v2.2.1 [44] generator. Matrix elements are calculated for up to two additional partons at NLO and four partons at LO using the

Comix [45] and OpenLoops [46] matrix element generators and are merged with the SHERPA PS [47] using the ME+PS@NLO prescription [48]. The NNPDF30NNLO [36] PDF set is used in conjunction with a dedicated PS tune developed by the SHERPA authors. Diboson processes are also simulated using the SHERPA generator using the NNPDF30NNLO PDF set in conjunction with a dedicated PS tune developed by the SHERPA authors. They are calculated for up to one (ZZ) or zero (WW, WZ) additional partons at NLO and up to three additional partons at LO. Other potential sources of backgrounds, such as the production of three or four top quarks or three gauge bosons, are found to be negligible. Finally, contributions from multijet background are estimated from data using a jet smearing procedure described in Ref. [49] and are found to be negligible in all regions.

All background processes are normalised to the best available theoretical calculation for their respective cross-sections. The NLO $t\bar{t}$ inclusive production cross section is corrected to the theory prediction at next-to-next-to-leading order (NNLO) in QCD including the resummation of next-to-next-to-leading logarithmic (NNLL) soft-gluon terms calculated using Top++2.0 [50–56]. Samples of single-top-quark events are normalised to the NLO cross-sections reported in Refs. [57–59].

For all samples, except those generated using SHERPA, the EvtGen v1.2.0 [60] program is used to simulate the properties of the bottom- and charm-hadron decays. All simulated events include a modelling of contributions from pileup by overlaying minimum-bias pp interactions from the same (in-time pileup) and nearby (out-of-time pileup) bunch crossings simulated in PYTHIA v8.186 and EvtGen v1.2.0 with the A2 [61] tune and MSTW2008LO PDF set [62].

4 Event reconstruction

This search is based upon a selection of events with many b-jets, large missing transverse momentum and no charged leptons (electrons and muons) in the final state. All events are required to have a reconstructed primary vertex which is consistent with the beamspot envelope and consists of at least two associated tracks in the inner detector with $p_{\mathrm{T}} > 500\,\mathrm{MeV}$. If more than one vertex passing the above requirements is found, the one with the largest sum of the squares of transverse momenta of associated tracks [63] is chosen.

Jet candidates are reconstructed from three-dimensional clusters of energy in the calorimeter [64] with the anti-k_t jet algorithm [65, 66] using a radius parameter of 0.4. The application of a jet energy scale (JES) correction derived from data and simulation [67] is used to calibrate the reconstructed jets. A set of quality criteria are applied to identify jets which arise from non-collision sources or detector noise [68] and any event which contains a jet failing this criteria is removed. Additional jets that arise from pileup interactions are rejected by applying additional track-based selections to jets with $p_{\mathrm{T}} < 120$ GeV and $|\eta| < 2.4$ and the jet momentum is corrected by subtracting the expected average energy contribution from pileup using the jet area method [69]. Jets are classified as either "baseline" or "signal", with baseline jets required to have $p_{\mathrm{T}} > 20$ GeV and $|\eta| < 4.8$. Signal jets are selected after resolving overlaps with electrons and muons, as described later in this section, and must pass tighter requirements of $p_{\mathrm{T}} > 30$ GeV and $|\eta| < 2.8$.

Signal jets are identified as b-jets if they are within $|\eta| < 2.5$ and are tagged by a multivariate algorithm which uses a selection of inputs including information about the impact parameters of inner detector tracks, the presence of displaced secondary vertices and the reconstructed flight paths of b- and c-hadrons inside the jet [70]. The b-tagging requirement with 77% efficiency, as determined in a sample of simulated $t\bar{t}$

events, was chosen as part of the optimisation procedure; where the corresponding mis-identification rate is 25% for c-jets and 0.88% for light-jets. To compensate for differences between data and MC simulation in the b-tagging efficiencies and mis-tag rates, correction factors are derived from data and applied to the samples of simulated events [70].

Electron candidates are reconstructed from energy clusters in the electromagnetic calorimeter matched to a track in the inner detector and are required to satisfy a set of "loose" quality criteria [71, 72]. They are also required to lie within the fiducial volume $|\eta| < 2.47$ and have $p_{\mathrm{T}} > 4.5$ GeV. Muon candidates are reconstructed by matching tracks in the inner detector with tracks in the muon spectrometer. Muon candidates which have a transverse (longitudinal) impact parameter with respect to the primary vertex larger than 0.2 mm (1 mm) are rejected to suppress muons from cosmic rays. Muon candidates are also required to satisfy "medium" quality criteria [73] and have $|\eta| < 2.5$ and $p_{\mathrm{T}} > 4$ GeV. Electron (muon) candidates are matched to the primary vertex by requiring the transverse impact parameter (d_0) to satisfy $|d_0|/\sigma(d_0) < 5(3)$, and the longitudinal impact parameter (z_0) to satisfy $|z_0 \sin\theta| < 0.5$ mm. Lepton candidates remaining after resolving overlaps with baseline jets are called "baseline" leptons. In the control regions where tighter lepton identification is required, "signal" leptons are chosen from the baseline set with $p_{\mathrm{T}} > 20$ GeV and are required to be isolated from other activity in the detector using a criterion designed to accept at least 95% of leptons from Z boson decays as detailed in Ref. [74]. In the control region where the single-lepton triggers are used, the leading lepton is required to have $p_{\mathrm{T}} > 27$ GeV to ensure full efficiency of the single-lepton triggers. Signal electrons are further required to satisfy "tight" quality criteria [71]. The MC events are corrected to account for differences in the lepton trigger, reconstruction and identification efficiencies between data and MC simulation.

Possible reconstruction ambiguities between baseline electrons, muons and jets are resolved by firstly removing electron candidates which share an inner detector track with a muon candidate. Jet candidates are then removed if they are within $\Delta R = \sqrt{(\Delta y)^2 + (\Delta\phi)^2} < 0.2$ of an electron candidate; next electron candidates are discarded if they are within $\Delta R = 0.4$ of a jet. Muons are discarded if they lie within $\Delta R = 0.4$ of any remaining jet, except for the case where the number of tracks associated with the jet is less than three, where the muon is kept and the jet is discarded.

Identified τ leptons decaying hadronically are not considered but the following τ-veto procedure is applied to reject events which contain τ-like objects. Candidates (τ_{cand}) are identified as jet candidates which have $|\eta| < 2.5$ and less than five inner detector tracks of $p_{\mathrm{T}} > 500$ MeV. If an event contains a tau candidate with a small azimuthal distance to the $\mathbf{p}_{\mathrm{T}}^{\mathrm{miss}}$ ($\Delta\phi(E_{\mathrm{T}}^{\mathrm{miss}}, \tau_{\mathrm{cand}}) < \pi/3$), then the event is vetoed.

The missing transverse momentum $\mathbf{p}_{\mathrm{T}}^{\mathrm{miss}}$ is defined as the negative vector sum of the p_{T} of all selected and calibrated physics objects (electrons, muons, photons [75] and jets) in the event, with an extra term added to account for soft energy in the event which is not associated with any of the selected objects [76]. This soft term is calculated from inner detector tracks with p_{T} above 500 MeV matched to the primary vertex to make it more robust against pileup contamination [77, 78].

5 Analysis strategy

Three sets of non-orthogonal signal regions (SRs) are defined and optimized to target different mass hierarchies of the SUSY particles involved. They exploit various discriminating observables and algorithms developed to explicitly reconstruct Higgs boson candidates in the decay chain. Events with charged leptons are vetoed in all SRs. Events with one, or two, charged leptons are used to define control regions (CRs)

employed to aid in the estimate of the main SM backgrounds. Additionally, events with zero charged leptons are utilised to define validation regions (VRs) to ensure the background estimation method is robust. The method for estimating these backgrounds is described in Section 6. The optimisation procedure for the event selection, aiming to maximize the efficiency to retain bottom-squark pair production events and reduce SM background contributions, is performed considering the two simplified model scenarios introduced in Section 1. As the $h \rightarrow bb$ decay mode is considered, the final state contains a large jet multiplicity, with many of these jets originating from b-quarks, and large $E_{\mathrm{T}}^{\mathrm{miss}}$ from the neutralinos.

The event selection criteria are defined on the basis of kinematic requirements for the objects described in the previous section and event variables described below. For these definitions, signal jets are used and are ordered according to decreasing p_{T}.

- N_{jets}: the number of signal jets.
- $N_{\mathrm{b-jets}}$: the number of b-jets.
- $\min \Delta\phi(\mathrm{jet}_{1-4}, \mathbf{p}_{\mathrm{T}}^{\mathrm{miss}})$: the minimum azimuthal distance between the four highest-p_{T} jets and the $\mathbf{p}_{\mathrm{T}}^{\mathrm{miss}}$ proves to be a powerful discriminating variable against multijet background events containing a large amount of $E_{\mathrm{T}}^{\mathrm{miss}}$ due to mismeasured jets. Typically, multijet background events exhibit low values of this variable and studies using data-driven multijet estimates indicate that a selection of $\min \Delta\phi(\mathrm{jet}_{1-4}, \mathbf{p}_{\mathrm{T}}^{\mathrm{miss}}) > 0.4$ is sufficient to reduce the multijet background to a negligible level.
- $\Delta\phi(j_1, \mathbf{p}_{\mathrm{T}}^{\mathrm{miss}})$: the azimuthal distance between the highest-p_{T} jet and the $\mathbf{p}_{\mathrm{T}}^{\mathrm{miss}}$. This variable is used to select events where the $\mathbf{p}_{\mathrm{T}}^{\mathrm{miss}}$ is expected to be recoiling against the leading jet.
- m_{eff}: the effective mass [79] of an event is defined as the scalar sum of the p_{T} of all signal jets and the $E_{\mathrm{T}}^{\mathrm{miss}}$, i.e.:

$$m_{\mathrm{eff}} = \sum_{i \leq N_{\mathrm{jets}}} (p_{\mathrm{T}}^{\mathrm{jet}})_i + E_{\mathrm{T}}^{\mathrm{miss}}. \tag{1}$$

- $\mathcal{S}$: referred to as the object-based $E_{\mathrm{T}}^{\mathrm{miss}}$ significance [80] and defined as follows: σ_{L} is the total expected longitudinal (parallel to the $\mathbf{p}_{\mathrm{T}}^{\mathrm{miss}}$) momentum resolution of all jets and leptons at a given p_{T} and $|\eta|$. It is parameterised using Monte Carlo simulation which well reproduces the resolution measured in data and is projected onto a basis parallel and transverse to the $\mathbf{p}_{\mathrm{T}}^{\mathrm{miss}}$. The quantity ρ_{LT} is a correlation factor between each jet's or lepton's longitudinal and transverse momentum resolution (again with respect to the $\mathbf{p}_{\mathrm{T}}^{\mathrm{miss}}$). $\mathcal{S}$ is used to discriminate events where the $E_{\mathrm{T}}^{\mathrm{miss}}$ arises from invisible particles in the final state from events where the $E_{\mathrm{T}}^{\mathrm{miss}}$ arises from poorly measured particles (and jets). Additionally it is useful to discriminate between signal events with large $E_{\mathrm{T}}^{\mathrm{miss}}$ and Z+jets events with medium-to-low $E_{\mathrm{T}}^{\mathrm{miss}}$. It is defined as:

$$\mathcal{S} = \sqrt{\frac{|\mathbf{p}_{\mathrm{T}}^{\mathrm{miss}}|^2}{\sigma_{\mathrm{L}}^2(1-\rho_{\mathrm{LT}}^2)}}. \tag{2}$$

Additional selections on the p_{T} of the leading jet and of the leading b-jet are also applied as detailed in the following sub-sections. In all signal regions, events containing baseline leptons with $p_{\mathrm{T}} > 10$ GeV are vetoed, as well as events containing τ-lepton candidates that align with the $\mathbf{p}_{\mathrm{T}}^{\mathrm{miss}}$ as described in Section 4. Only events with $E_{\mathrm{T}}^{\mathrm{miss}} > 250$ GeV are retained to ensure full efficiency of the trigger.

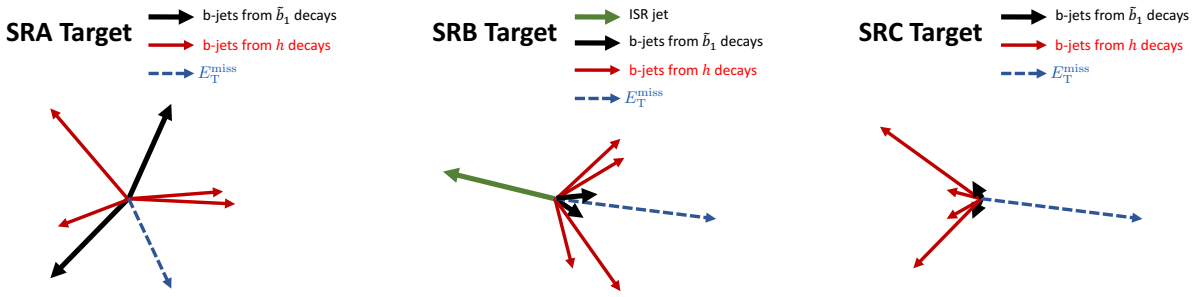

(a) SRA (b) SRB (c) SRC

Figure 2: The different event kinematics targeted by the three SRs: (a) kinematics in the bulk region, with high p_{T} b-jets arising from the bottom-squark decay; (b) kinematics in the compressed region of the $\Delta m(\tilde{\chi}_2^0, \tilde{\chi}_1^0) = 130\,\mathrm{GeV}$ scenario with soft b-jets from the bottom-squark; (c) kinematics in the compressed region of the $m(\tilde{\chi}_1^0) = 60\,\mathrm{GeV}$ scenario which also contains soft b-jets from the bottom-squark.

The event kinematics targeted by the three SRs are depicted in Figure 2. The SRA region targets the "bulk" region of both signal mass scenarios, with moderate- to high-mass splitting between the $\tilde{b}_1$ and $\tilde{\chi}_2^0$. In these scenarios all of the b-jets, from both the bottom-squark and Higgs boson decays, are at a relatively high p_{T} and can be resolved in the detector. The b-jets from the Higgs boson can be isolated by removing the ones most likely from the bottom-squark decays and checking the angular separation between the remaining b-jets. The SRB region targets the phase space of the $\Delta m(\tilde{\chi}_2^0, \tilde{\chi}_1^0) = 130\,\mathrm{GeV}$ scenario with a small mass splitting between the $\tilde{b}_1$ and $\tilde{\chi}_2^0$, referred to as the "compressed" region. An initial-state radiation (ISR)-like selection is used where the small mass splitting between the bottom-squark and neutralino leads to very soft b-jets from the bottom-squark decay, which are difficult to reconstruct. In this scenario it is possible to reconstruct both Higgs bosons using angular separation methods. Finally, the SRC region targets the "compressed" region of the $m(\tilde{\chi}_1^0) = 60\,\mathrm{GeV}$ signal scenario, where the mass splitting between the $\tilde{b}_1$ and $\tilde{\chi}_2^0$ is small. The b-jets from the bottom-squark decay are relatively soft and as such a lower b-jet multiplicity is used in this region, when compared to the A- and B-type selections. Additionally, the visible system (b-jets from the bottom-squark decay and Higgs boson decay) is produced back-to-back with the reconstructed $\mathbf{p}_{\mathrm{T}}^{\mathrm{miss}}$.

5.1 The SRA selections

To exploit the kinematic properties of the signal over the large range of $\tilde{b}_1$, $\tilde{\chi}_2^0$ and $\tilde{\chi}_1^0$ masses explored, incremental thresholds are imposed on the main discriminating variable, m_{eff}, resulting in three mutually exclusive regions, $1.0 < m_{\mathrm{eff}} < 1.5\,\mathrm{TeV}$, $1.5 < m_{\mathrm{eff}} < 2.0\,\mathrm{TeV}$ and $m_{\mathrm{eff}} > 2.0\,\mathrm{TeV}$ labelled as SRA-L, -M and -H, respectively, to maximise coverage across the $\tilde{b}_1$ mass range. The selection criteria for the SRAs are summarised in Table 1. At least four b-tagged jets are required. To discriminate against multijet background, events where the $\mathbf{p}_{\mathrm{T}}^{\mathrm{miss}}$ is aligned with a jet in the transverse plane are rejected by requiring $\min \Delta\phi(\mathrm{jet}_{1-4}, \mathbf{p}_{\mathrm{T}}^{\mathrm{miss}}) > 0.4$. As a large $E_{\mathrm{T}}^{\mathrm{miss}}$ is expected from the neutralinos which escape the detector, a selection of $E_{\mathrm{T}}^{\mathrm{miss}} > 350\,\mathrm{GeV}$ is used. Additionally, the leading b-jet (b_1) is expected to have a large p_{T}, hence a selection of $p_{\mathrm{T}}(b_1) > 200\,\mathrm{GeV}$ is employed. At least one of the two Higgs boson candidates in

the event is identified using a single Higgs boson reconstruction algorithm referred to as *max-min*, which is detailed in the following. The expected signal topology is exploited using a two-step procedure to first attempt to remove the high-p_{T} b-jets from the bottom-squark decay, then using the remaining b-jets to reconstruct a Higgs boson in the decay chain. This procedure is implemented as follows: first, pairs of b-jets are formed by iterating through all of the b-jets in the event, and the one with the largest separation in ΔR is designated as arising from the bottom-squark decay; second, among the remaining pairs, the one with lowest ΔR is identified as a possible Higgs boson candidate and its invariant mass calculated. The following ΔR and mass quantities are defined:

- $\Delta R_{\mathrm{max}}(b, b)$: the distance in η–ϕ between the two b-jets with the maximal angular separation which are most likely to originate from the initial decay of the $\tilde{b}_1$;
- $\Delta R_{\mathrm{max-min}}(b, b)$: the distance in η–ϕ between the two b-jets with the minimum angular separation which are most likely to originate from the same Higgs boson decay, selected out of the remaining b-jets;
- $m(h_{\mathrm{cand}})$: the invariant mass of the two b-jets closest in angular separation, after performing the *max-min* algorithm, used to reconstruct the Higgs boson mass. A lower bound on $m(h_{\mathrm{cand}})$ is used, as for the majority of signals the distribution peaks around the Higgs boson mass, but in scenarios where the incorrect combination of b-jets is chosen the signal can extend to higher masses.

When applied to signal, the algorithm correctly selects a $h \rightarrow bb$ pairing in 20 to 40% of cases, for a single higgs decay, depending upon the model. For a signal model corresponding to $m(\tilde{b}_1, \tilde{\chi}_2^0, \tilde{\chi}_1^0) = (1100, 330, 200)$ GeV, about 3% of the simulated signal events are retained by the SRA selections.

Table 1: Signal region definitions for the inclusive A-type SR, alongside the three varying m_{eff} intervals used. The letter appended to the SRA label corresponds to the low, medium or high m_{eff} selection. This selection is sensitive to the bulk regions of both signal scenarios. The jets and b-jets are ordered by p_{T}.

Variable	SRA	SRA-L	SRA-M	SRA-H
N_{leptons} (baseline)	$= 0$		$= 0$	
N_{jets}	≥ 6		≥ 6	
$N_{\mathrm{b-jets}}$	≥ 4		≥ 4	
$E_{\mathrm{T}}^{\mathrm{miss}}$ [GeV]	> 350		> 350	
$\min \Delta\phi(\mathrm{jet}_{1-4}, \mathbf{p}_{\mathrm{T}}^{\mathrm{miss}})$ [rad]	> 0.4		> 0.4	
τ veto	Yes		Yes	
$p_{\mathrm{T}}(b_1)$ [GeV]	> 200		> 200	
$\Delta R_{\mathrm{max}}(b, b)$	> 2.5		> 2.5	
$\Delta R_{\mathrm{max-min}}(b, b)$	< 2.5		< 2.5	
$m(h_{\mathrm{cand}})$ [GeV]	> 80		> 80	
m_{eff} [TeV]	> 1.0	$\in [1.0, 1.5]$	$\in [1.5, 2.0]$	> 2.0

5.2 The SRB selections

The SRB region targets small mass-splitting between the $\tilde{b}_1$and $\tilde{\chi}_2^0$ (order 5–20 GeV), in the case of the $\Delta m(\tilde{\chi}_2^0, \tilde{\chi}_1^0) = 130$ GeV scenarios. The presence of an ISR jet boosting the bottom-squarks, and consequently their decay products, is exploited. To efficiently suppress SM background contributions,

events are selected where the highest p_{T} jet is not b-tagged and has $p_{\mathrm{T}} > 350\,\mathrm{GeV}$, this jet is presumed to arise from ISR in the scenario under consideration. Additional selections of $E_{\mathrm{T}}^{\mathrm{miss}} > 350$ GeV and $\Delta\phi(j_1, E_{\mathrm{T}}^{\mathrm{miss}}) > 2.8$ are also applied. An m_{eff} selection of $> 1\,\mathrm{TeV}$ is also applied. As the b-jets from $\tilde{b}_1$decays might have too low momenta to pass the b-jet requirements, a different algorithm, aiming to reconstruct both Higgs boson candidates, is employed.

Differently from the scenarios targeted by SRA, pairs of b-jets with the largest ΔR are found to be more likely to arise from the decay of the same Higgs boson candidate. Two pairs at a time are identified following an iterative procedure, ΔR_{bb1} and ΔR_{bb2}. The efficiency of correctly selecting the b-jets using this algorithm is in the range 15–30%. The average mass of the two candidates $m(h_{\mathrm{cand1}}, h_{\mathrm{cand2}})_{\mathrm{avg}}$ is calculated and a requirement is placed on the average mass, corresponding to a window around the Higgs boson mass: [75, 175] GeV. For a signal model corresponding to $m(\tilde{b}_1, \tilde{\chi}_2^0, \tilde{\chi}_1^0) = (700, 680, 550)\,\mathrm{GeV}$, about 0.1% of the simulated signal events are retained by the SRB selections. The SRB requirements are listed in Table 2.

Table 2: Signal region definition for the B-type SR, targeting the compressed region of the $\Delta m(\tilde{\chi}_2^0, \tilde{\chi}_1^0) = 130\,\mathrm{GeV}$. The jets and b-jets are ordered by p_{T}.

Variable	SRB
N_{leptons} (baseline)	$= 0$
N_{jets}	≥ 5
$N_{\mathrm{b-jets}}$	≥ 4
$E_{\mathrm{T}}^{\mathrm{miss}}$ [GeV]	> 350
$\min \Delta\phi(\mathrm{jet}_{1-4}, \mathbf{p}_{\mathrm{T}}^{\mathrm{miss}})$ [rad]	> 0.4
τ veto	Yes
$m(h_{\mathrm{cand1}}, h_{\mathrm{cand2}})_{\mathrm{avg}}$ [GeV]	$\in [75, 175]$
leading jet not b-tagged	Yes
$p_{\mathrm{T}}(j_1)$ [GeV]	> 350
$\lvert\Delta\phi(j_1, E_{\mathrm{T}}^{\mathrm{miss}})\rvert$ [rad]	> 2.8
m_{eff} [TeV]	> 1

5.3 The SRC selections

When considering the scenario with a constant $\tilde{\chi}_1^0$ mass of 60 GeV, the ΔR-based algorithms to reconstruct the Higgs boson candidates are ineffective in the compressed region of phase space with a small mass splitting between the $\tilde{b}_1$ and $\tilde{\chi}_2^0$. In the inclusive SRC, events are required to have at least three b-jets whilst the main discriminating quantity is $\mathcal{S}$, where a selection of $\mathcal{S} > 22$ is employed. Additionally, four non-overlapping regions (SRC22, SRC24, SRC26 and SRC28) are defined as sub-sets of the inclusive SRC region, with incremental thresholds on $\mathcal{S}$ as reported in Table 3, to ensure full coverage of the target models as a function of bottom-squark and neutralino mass. For a signal model corresponding to $m(\tilde{b}_1, \tilde{\chi}_2^0, \tilde{\chi}_1^0) = (1200, 1150, 60)\,\mathrm{GeV}$, about 11% of the simulated signal events are retained by the SRC selections. The $\mathcal{S}$ variable is effective in rejecting the SM background arising from associated production of a Z boson decaying to neutrinos and heavy-flavour jets.

Table 3: Signal region selections for the C-type SRs targeting the region with small mass splitting between the $\tilde{b}_1$ and $\tilde{\chi}_2^0$, in the $m(\tilde{\chi}_1^0) = 60\,\text{GeV}$ signal scenario. The jets and b-jets are ordered by p_{T}.

Variable	SRC	SRC22	SRC24	SRC26	SRC28
N_{leptons} (baseline)	$= 0$	$= 0$			
N_{jets}	≥ 4	≥ 4			
$N_{\text{b-jets}}$	≥ 3	≥ 3			
$E_{\text{T}}^{\text{miss}}$ [GeV]	> 250	> 250			
$\min \Delta\phi(\text{jet}_{1-4}, \mathbf{p}_{\text{T}}^{\text{miss}})$ [rad]	> 0.4	> 0.4			
$\mathcal{S}$	> 22	$\in [22, 24]$	$\in [24, 26]$	$\in [26, 28]$	> 28

6 Background estimation

There are two main SM backgrounds which are expected to contribute to the yields for the SRs introduced in the previous section. For the SRA and SRB regions, the main background is $t\bar{t}$, which contributes between 70–85% depending upon the region considered, and it is dominated by top-quark pairs produced in association with two b-quarks arising from gluon splitting. For the SRC regions the main backgrounds arise from top-quark related processes ($t\bar{t}$ and single-top) and Z+jets. In all C-type regions the Z+jets background is dominant (between 39–47% depending upon the region) with the subdominant contribution arising from the top-quark backgrounds (12–21%).

The main SM backgrounds in each SR are determined separately with a profile likelihood fit to the event yields in the associated CRs [81]. This is commonly referred to as a background-only fit which constrains and adjusts the normalisation of the background processes. The background-only fit uses the observed event yield and the number of expected MC events in the associated CRs, which are described by Poisson statistics, as a constraint to adjust the normalisation of the background processes assuming that no signal is present. The normalisation factor is referred to as the μ factor. The CRs are designed to be enriched in specific background contributions relevant to the analysis, whilst minimising the potential signal contamination, and they are orthogonal to the SRs. When performing the fit for the A-type SR, a multi-bin approach is used, with a single CR divided into three bins of m_{eff}. Such an approach allows for the calculation of a single normalisation parameter (to apply to the main $t\bar{t}$ background across all bins of m_{eff}) and additionally allows for the fit to take into account the modelling of the m_{eff} variable. The systematic uncertainties, described in Section 7, are included in the fit as nuisance parameters. They are constrained by Gaussian distributions with widths corresponding to the sizes of the uncertainties and are treated as correlated, when appropriate, between the various regions. The product of the various probability density functions and the Gaussian distributions forms the likelihood function, which the fit maximizes by adjusting the background normalisation and the nuisance parameters. This approach reduces the influence of systematic uncertainties on the backgrounds which have associated CRs, as these are absorbed by the normalisation parameter. Finally, the reliability of the MC extrapolation of the SM background estimates outside of the control regions is evaluated in dedicated VRs orthogonal to CRs and SRs.

The fit strategies for the A- and B-type regions are very similar and are schematically represented in Figure 3(a). They rely on CRs with a single lepton requirement, as the $t\bar{t}$ background in the SR is dominated by semi-leptonic $t\bar{t}$ decays where the lepton is not identified. The main background in both regions is $t\bar{t}$ pair production in association with heavy-flavour jets. The fit strategy for the C-type regions is presented in

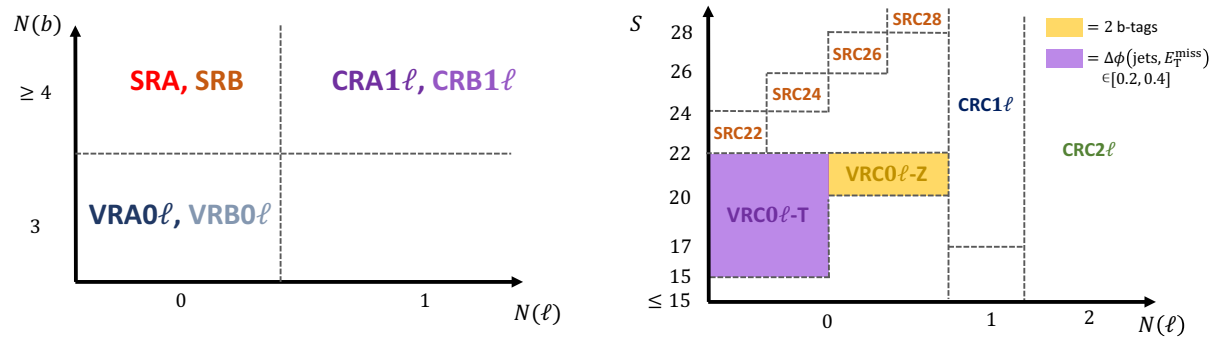

(a) A- and B-type fit strategy

(b) C-type fit strategy

Figure 3: Schematic diagrams of the fit strategies for (left) the A-, B- and (right) C-type regions. Generally the CRs require a different lepton multiplicity than the SRs. The validation regions are defined with a lower b-jet multiplicity requirement, except in the case of the VRC0ℓ-T region, which instead inverts the SR min $\Delta\phi(\text{jet}_{1-4}, \mathbf{p}_{\text{T}}^{\text{miss}})$ selection.

Figure 3(b). The strategy is different as the main background in these regions is Z+jets, closely followed by the top-quark backgrounds. In order to define CRs enhanced in $t\bar{t}$ and Z+jets, additional variables are used:

- m_{T} : the event transverse mass m_{T} is defined as $m_{\text{T}} = \sqrt{2p_{\text{T}}(\ell)E_{\text{T}}^{\text{miss}}(1-\cos(\Delta\phi))}$, where $\Delta\phi$ is the difference in azimuthal angle between the lepton and the $\mathbf{p}_{\text{T}}^{\text{miss}}$, and is used in the one-lepton CRs to reject multi-jet events which can be mis-identified as containing a prompt lepton.
- $m_{\ell\ell}$: the invariant mass of the two leptons in the event. As the 2L CR is used to constrain the Z+jets background, the $m_{\ell\ell}$ variable is required to be within the Z-mass window: [86, 106] GeV (used exclusively in the two-lepton CR).
- $\tilde{E}_{\text{T}}^{\text{miss}}$: the "lepton corrected" $E_{\text{T}}^{\text{miss}}$. For the 2L CR the transverse momentum vectors of the leptons are subtracted from the $E_{\text{T}}^{\text{miss}}$ calculation in order to mimic the neutrinos from $Z \to \nu\nu$ decays (used exclusively in the two-lepton CR).

When designing the CRs and VRs, the potential signal contamination is checked in each region to ensure that the contribution from the signal process being targeted is small in the regions. The signal contamination in the CRs and VRs is found to be negligible, at the level of $< 1\%$ of the total SM expectation, depending upon the signal mass hierarchy of the models considered in this search.

6.1 A-type CR and VR definitions

A single control region, which is $t\bar{t}$-dominated (CRA1ℓ), is defined for the A-type regions. As previously mentioned the inclusive SRA is further split into three orthogonal m_{eff} selections enabling a multi-bin fit to be performed. As such the CRA1ℓ is additionally split into the same three identical m_{eff} selections as the SR. The CR is defined similarly to the SR selection (as documented in Table 1). However, a single signal lepton (either e or μ), with $p_{\text{T}} > 20$ GeV is required in the final state. Furthermore, the selections used to isolate the Higgs boson in the SRAs, namely the $\Delta R_{\text{max}}(b,b)$, $\Delta R_{\text{max-min}}(b,b)$ and $m(h_{\text{cand}})$ selections, are not applied in order to increase the number of events in the CR. The leading b-jet p_{T} selection is lowered to > 100 GeV to further increase the number of events in the region, and a selection on the transverse

mass of $m_{\mathrm{T}} > 20\,\mathrm{GeV}$ is applied to suppress mis-identified leptons. Such selections result in very pure $t\bar{t}$ CRs, with $t\bar{t}$ contributing more than 80% of the total SM contribution in each of the CRs. The fraction of top-quark pairs produced in association with b-quarks is equivalent to the one of the SRs, and accounts for about 70% of the total $t\bar{t}$ contributions. Figure 4(a) presents the distribution of $m(h_{\mathrm{cand}})$ in the CRA1ℓ, and shows that this variable is well modelled.

A zero-lepton validation region (VRA0ℓ) is defined, which is also split into the same m_{eff} thresholds as the SR and CR, and is used to validate the modelling of the $t\bar{t}$ when extrapolating from the one-lepton CRs to zero-lepton regions. The selections are based upon the SR selections but the VRs are orthogonal due to the b-jet multiplicity selection which requires exactly 3 b-jets. Additionally, the $\Delta R_{\mathrm{max}}(b,b)$, $\Delta R_{\mathrm{max-min}}(b,b)$ and $m(h_{\mathrm{cand}})$ selections are not applied in this region. A selection of $\mathcal{S} < 22$ is applied to ensure this region is orthogonal to the SRC regions.

6.2 B-type CR and VR definitions

For the B-type $t\bar{t}$ CR (CRB1ℓ), a similar method of using a one-lepton region enriched in $t\bar{t}$ is implemented. The SR selections (as documented in Table 2) are applied, and additionally a single signal lepton with $p_{\mathrm{T}} > 20\,\mathrm{GeV}$ is required. The $m(h_{\mathrm{cand1}}, h_{\mathrm{cand2}})_{\mathrm{avg}}$ selection is dropped to increase the number of events in the region, and the $|\Delta\phi(j_1, E_{\mathrm{T}}^{\mathrm{miss}})|$ selection is loosened to > 2.2. Similarly to the A-type CR, a selection of $m_{\mathrm{T}} > 20\,\mathrm{GeV}$ is applied to suppress mis-identified leptons. These selections result in a CR which is very pure with 80% of the total SM expectation consisting of $t\bar{t}$. Figure 4(b) presents the $m(h_{\mathrm{cand1}}, h_{\mathrm{cand2}})_{\mathrm{avg}}$ distribution in this region, which is shown to be well modelled.

The associated VR (VRB0ℓ) is defined in a similar manner to the A-type VR, with similar selections to the SRB region, but an exclusive b-jet multiplicity selection of exactly three b-jets. Additionally the selections used to reconstruct the Higgs bosons in the event are dropped to enhance the number of events in the region. A selection of $\mathcal{S} < 22$ is also applied to ensure this region is orthogonal to the C-type SRs.

6.3 C-type CR and VR definitions

Two CRs are defined for the C-type SRs, one to constrain the Z+jets background (CRC2ℓ) and one to constrain the backgrounds associated with top-quarks, $t\bar{t}$ and single-top, (CRC1ℓ). A single normalisation parameter is used to constrain both $t\bar{t}$ and single-top backgrounds, while the $Z+$jets background is constrained with an additional normalisation parameter. These CRs are based upon the SR shown in Table 3, but are orthogonal due to the different lepton multiplicities required.

The CRC2ℓ requires two same-flavour (SF) opposite-sign (OS) leptons, with invariant mass in the Z-mass window. The leading lepton is required to have $p_{\mathrm{T}} > 27\,\mathrm{GeV}$ while the secondary lepton is required to have $p_{\mathrm{T}} > 20\,\mathrm{GeV}$. To imitate the $E_{\mathrm{T}}^{\mathrm{miss}}$ selection in the SR, in this 2L CR a selection of $\tilde{E}_{\mathrm{T}}^{\mathrm{miss}} > 250\,\mathrm{GeV}$ is utilised. For this region the selections on $\mathcal{S}$ are dropped to enhance the number of events in the region. Figure 4(c) shows the $\tilde{E}_{\mathrm{T}}^{\mathrm{miss}}$ distribution in this region. The CRC1ℓ region used to constrain the top-quark-related backgrounds requires one signal lepton with $p_{\mathrm{T}} > 20\,\mathrm{GeV}$. A lower limit on $\mathcal{S}$ of > 17 is applied. Similarly as with the A- and B-type CR, a selection of $m_{\mathrm{T}} > 20\,\mathrm{GeV}$ is applied to remove the multi-jet contribution with fake or non-prompt leptons. Figure 4(d) presents the $\mathcal{S}$ distribution in this region.

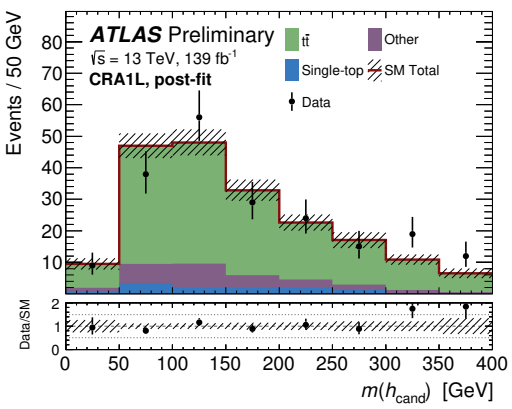

(a) $m(h_{\text{cand}})$ in CRA1ℓ

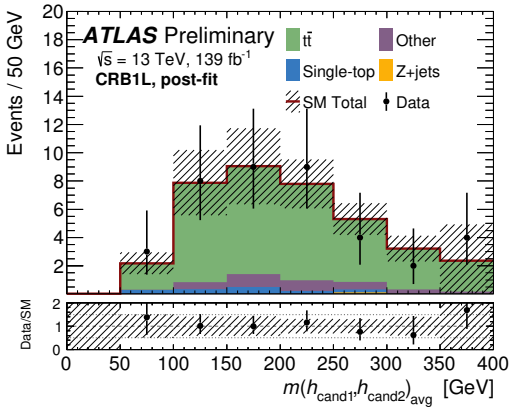

(b) $m(h_{\text{cand1}}, h_{\text{cand2}})_{\text{avg}}$ in CRB1ℓ

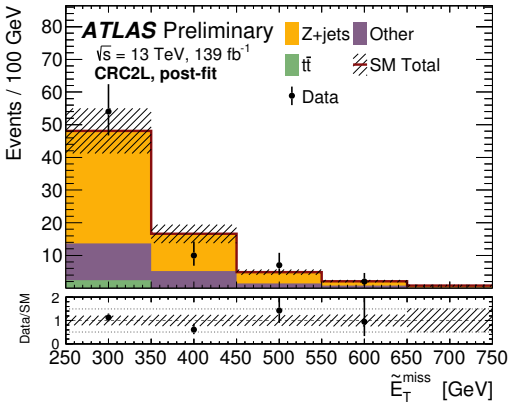

(c) $\tilde{E}_{\text{T}}^{\text{miss}}$ in CRC2ℓ

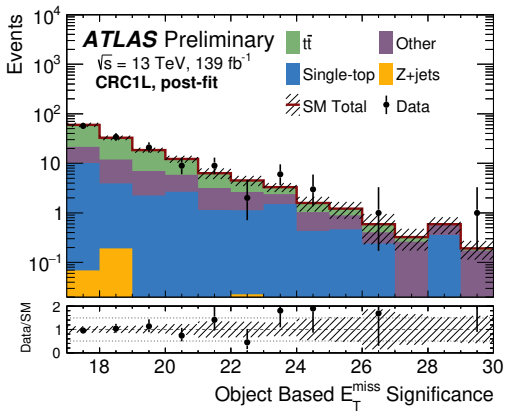

(d) $\mathcal{S}$ in CRC1ℓ

Figure 4: Distributions of (a) the $m(h_{\text{cand}})$ in CRA1ℓ, (b) the $m(h_{\text{cand1}}, h_{\text{cand2}})_{\text{avg}}$ in CRB1ℓ, (c) $\tilde{E}_{\text{T}}^{\text{miss}}$ in CRC2ℓ, and (d) $\mathcal{S}$ in CRC1ℓ after the background-only fit; ratios between SM predictions and data are reported in the bottom panels. All uncertainties as defined in Section 7 are included in the uncertainty bands of top and bottom panels in each plot. The backgrounds which contribute only a small amount (diboson, W+jets and $t\bar{t}+W/Z/h$) are grouped and labelled as "Other". Overflow events which do not fall into the axis range are placed into the right-most bin.

Two zero-lepton VRs are defined to validate the extrapolation from CR to SR based upon the SR selections. A selection requiring zero-leptons, two b-jet VR (VRC0ℓ-Z) with $\mathcal{S} \in [20, 22]$, and $E_{\text{T}}^{\text{miss}} \in [250, 600]$ GeV ensures a region orthogonal to the SR, but with a large contribution from the Z+jets process. The second VR is used to validate the modelling of the $t\bar{t}$ and single-top backgrounds (VRC0ℓ-T), with zero leptons, $\mathcal{S} \in [15, 22]$ and an inverted selection on the min $\Delta\phi(\text{jet}_{1-4}, \mathbf{p}_{\text{T}}^{\text{miss}}) \in [0.2, 0.4]$ to ensure orthogonality.

6.4 Summary of CR and VR results

A full overview of the control and validation regions used in the analysis can be found in Table 4. The control region pre-fit yields and fitted normalisation factors μ_{bkg} for the A-, B- and C-type regions are

presented in Figure 5 (left). All μ values are consistent with unity, within 2 sigma of the normalisation uncertainty, suggesting good modelling of the key SM background processes already at the level of MC predictions. Figure 5 (right) presents the observed yields, post-fit background estimates and significance [82] for the A-, B- and C-type validation regions. The background-only fit estimates are in good agreement with the data in these regions, with the post-fit expectation within 1σ of the central value for all regions.

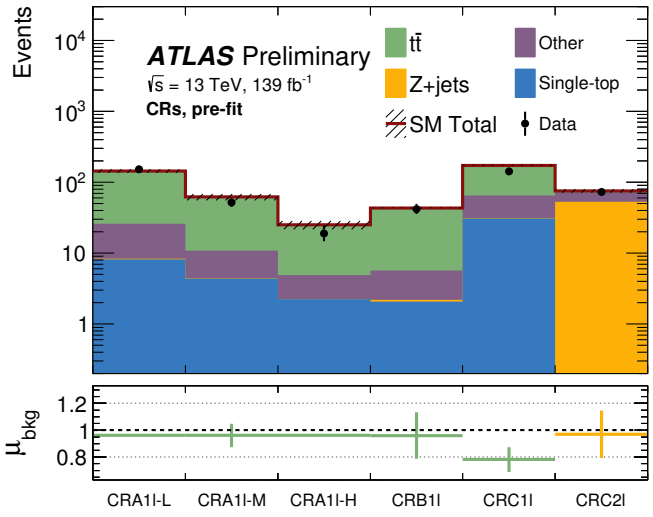

(a) Control region event pre-fit yields

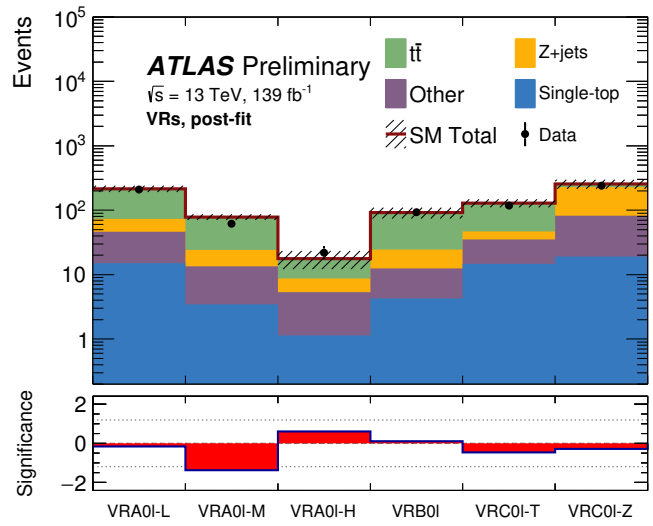

(b) Validation region post-fit results

Figure 5: (a) Control region event pre-fit yields compared to SM MC predictions (top panel) and μ scale factors (bottom panel) for the A-, B- and C-type regions. The uncertainty on the μ factors and the total expected yield include statistical and systematic uncertainties as introduced in Section 7. For the A-type regions, as the fit is performed in the m_{eff} intervals, the normalisation is applied to all bins equally. (b) Results of the background-only fit extrapolated to VRs for the A-, B- and C-type regions. The normalisation of the backgrounds is obtained from the fit to the CRs. The upper panel shows the observed number of events and the predicted background yields. Statistical and systematic uncertainties as introduced in Section 7 are included in the uncertainty band. The lower panel shows the significance in each VR. The significance calculation is performed as described in Ref. [82]. The backgrounds which contribute only a small amount (diboson, W+jets and $t\bar{t}+W/Z/h$) are grouped and labelled as "Other".

Table 4: Summary of all control and validation region definitions used in the analysis.

		Control Regions				Validation Regions			
Variable	Units	CRA1ℓ	CRB1ℓ	CRC1ℓ	CRC2ℓ	VRA0ℓ	VRB0ℓ	VRC0ℓ-T	VRC0ℓ-Z
$E_{\mathrm{T}}^{\mathrm{miss}}$ Trigger		✓	✓	✓	-	✓	✓	✓	✓
Lepton Trigger		-	-	-	✓	-	-	-	-
$E_{\mathrm{T}}^{\mathrm{miss}}$	[GeV]	> 250	> 300	> 250	< 70	> 350	> 350	> 250	$\in [250, 600]$
$\min[\Delta\phi(\mathrm{jet}_{1-4}, E_{\mathrm{T}}^{\mathrm{miss}})]$	[rad]	-	-	-	> 0.2	> 0.4	> 0.4	$\in [0.2, 0.4]$	> 1.2
N_{leptons} (baseline)		1	1	1	2	0	0	0	0
N_{leptons} (signal)		1	1	1	2 (SFOS)	-	-	-	-
$p_{\mathrm{T}}(\ell_1)$	[GeV]	> 20	> 20	> 20	> 27	-	-	-	-
$p_{\mathrm{T}}(\ell_2)$	[GeV]	-	-	-	> 20	-	-	-	-
m_{T}	[GeV]	> 20	> 20	> 20	-	-	-	-	-
$\mathrm{m}_{\ell\ell}$	[GeV]	-	-	-	$\in [86, 106]$	-	-	-	-
τ veto		-	✓	-	-	✓	✓	-	-
N_{jets}		≥ 6	≥ 4	≥ 4	≥ 4	≥ 6	≥ 4	≥ 4	≥ 4
$N_{\mathrm{b-jets}}$		≥ 4	≥ 4	≥ 3	≥ 3	3	3	≥ 3	2
$p_{\mathrm{T}}(b_1)$	[GeV]	> 100	-	-	-	> 100	-	-	-
$p_{\mathrm{T}}(j_1)$	[GeV]	-	> 350	-	-	-	> 350	-	-
leading jet not b-tagged		-	✓	-	-	-	✓	-	-
$\lvert\Delta\phi(j_1, E_{\mathrm{T}}^{\mathrm{miss}})\rvert$	[rad]	-	> 2.2	-	-	-	> 2.8	-	-
$\tilde{E}_{\mathrm{T}}^{\mathrm{miss}}$	[GeV]	-	-	-	> 250	-	-	-	-
$\mathcal{S}$		-	-	> 17	-	< 22	< 22	$\in [15, 22]$	$\in [20, 22]$
m_{eff}	[TeV]	> 1.0	> 1.0	-	-	> 1.0	> 1.0	-	-

7 Systematic uncertainties

Several sources of experimental and theoretical systematic uncertainty in the signal and background estimates are considered in this analysis. Their impact is reduced by fitting the event yields and normalising the dominant backgrounds in the control regions defined with kinematic selections resembling those of the corresponding signal regions (see Section 6). Uncertainties due to the numbers of events in the CRs are also introduced in the fit for each region. The magnitude of the contributions arising from detector, theoretical modelling and statistical uncertainties are summarized in Table 5.

Dominant detector-related systematic uncertainties arise from the b-tagging efficiency and mis-tagging rates, jet energy scale and jet energy resolution. In the SRA regions and the SRB region the contributions of these uncertainties are almost equivalent. In the SRC region the b-tagging uncertainty is dominant. The systematic uncertainty on the b-tagging efficiency ranges from 4.5% for b-jets with $p_{\mathrm{T}} \in [35, 40]$ GeV up to 7.5% for b-jets with larger p_{T} (> 100 GeV). It is estimated by varying the η-, p_{T}- and flavour-dependent scale factors applied to each jet in the simulation within a range that reflects the systematic uncertainty in the measured tagging efficiency and mis-tag rates in data [70]. The uncertainties in the jet energy scale and resolution are based on their respective measurements in data [67, 83]. The uncertainties associated with lepton reconstruction and energy measurements have a negligible impact on the final results. However, the lepton, photon and jet-related uncertainties are propagated to the calculation of the $E_{\mathrm{T}}^{\mathrm{miss}}$, and additional uncertainties are included in the energy scale and resolution of the soft term. The systematic uncertainties related to the modelling of the energy of jets and leptons in the simulation are propagated to $\mathcal{S}$. No additional uncertainty of the energy resolution is applied. This is because the resolutions are taken to be the maximum of the parameterised data and simulation resolutions when performing the calculation for both data and MC.

Uncertainties in the modelling of the SM background processes from MC simulation and their theoretical cross-section uncertainties are also taken into account. The dominant uncertainties in SRA and SRB arise from theoretical and modelling uncertainties of the top quark pair. They are computed as the difference between the prediction from nominal samples and those from additional samples differing in hard-scattering generator and parameter settings, or using internal weights assigned to the events depending on the choice of renormalisation and factorisation scales, initial- and final-state radiation parameters and PDF sets. The impact of the PS and hadronisation model is evaluated by comparing the nominal generator with a POWHEG sample interfaced to HERWIG 7 [84,85], using the H7UE set of tuned parameters [85]. To assess the uncertainty due to the choice of hard-scattering generator and matching scheme, an aMC@NLO+PYTHIA8 setup is employed. It uses the shower starting scale, $\mu_{\mathrm{q}} = H_{\mathrm{T}}/2$, where H_{T} is defined here as the scalar sum of the p_{T} of all outgoing partons.

The dominant uncertainties in SRC arise from the MC modelling of the Z+jets process, followed by uncertainties on $t\bar{t}$ and single-top. The Z+jets (as well as W+jets) modelling uncertainties are estimated by considering different merging (CKKW-L) and resummation scales using alternative samples, PDF variations from the NNPDF30NNLO replicas [44] and variations of factorisation and renormalisation scales in the ME. The latter have been evaluated using 7 point-variations, changing the renormalisation and factorisation scales up and down by factors 0.5 and 2, such as when one scale is up the other is down, and vice-versa.

For the SUSY signal processes, both the experimental and theoretical uncertainties in the expected signal yield are considered. Experimental uncertainties are found to be between 6% and 36% across the mass plane with fixed LSP mass for A-type SRs and between 4% and 40% for C-type SRs. For models where

$\Delta m(\tilde{\chi}_2^0, \tilde{\chi}_1^0) = 130$ GeV is assumed, scenarios where SRB is relevant have uncertainties between 11% and 37%. In all SRs, they are largely dominated by the uncertainty in the b-tagging efficiency. Theoretical uncertainties in the approximate NNLO+NNLL cross-section are calculated for each SUSY signal scenario and are dominated by the uncertainties in the renormalisation and factorisation scales, followed by the uncertainty in the PDF. They vary between 7% and 17% for bottom-squark masses in the range between 400 GeV and 1500 GeV. Additional uncertainties in the acceptance and efficiency due to the modelling of initial-state radiation and CKKW scale variations in SUSY signal MC samples are also taken into account and contribute up to about 10%.

Table 5: Dominant systematic uncertainties on background estimates in the A-type (inclusive), B-type and C-type (inclusive) regions. Individual uncertainties can be correlated, and do not necessarily add up quadratically to the total background uncertainty. The percentages show the size of the uncertainty relative to the total expected background.

Region	SRA	SRB	SRC
Total background expectation	17.1	3.3	37.9
Total background uncertainty	2.8 (16%)	0.9 (27%)	6.2 (16%)
Systematic, experimental	1.4 (8%)	0.3 (10%)	3.0 (8%)
Systematic, theoretical	2.3 (13%)	0.6 (18%)	3.2 (8%)
Statistical, MC samples	0.7 (4%)	0.4 (12%)	2.0 (5%)

8 Results and interpretation

The event yields for all signal regions are reported in Table 6. The SM background expectations resulting from background-only fits are also reported showing statistical plus systematic uncertainties. The largest background contribution in A-type and B-type SRs arises from $t\bar{t}$ production, whilst $Z \rightarrow \nu\bar{\nu}$ production in association with b-quarks is largest in the C-type SRs, with sub-dominant contributions from the $t\bar{t}$ and single-top processes. Other background sources are $t\bar{t}+W/Z$, $t\bar{t}+h$, diboson and W+jets production. The results are also summarized in Figure 6, where the significances for each of the SRs are also presented. No significant deviations are observed between expected and observed yields in all signal regions considered.

Figure 7 shows the comparison between the observed data and the post-fit SM predictions for some relevant kinematic distributions for the inclusive SRA, SRB and SRC selections before specific requirements are applied on the quantity shown. For illustrative purposes, the distributions expected for scenarios with different bottom-squark, $\tilde{\chi}_2^0$ and $\tilde{\chi}_1^0$ masses depending on the SR considered are shown.

The CL_s technique [86] is used to place 95% Confidence Level (CL) upper limits on event yields from physics beyond the SM (BSM) for each signal region. The profile-likelihood-ratio test statistic is used to exclude the signal-plus-background hypothesis for specific signal models. When normalised to the integrated luminosity of the data sample, results can be interpreted as corresponding upper limits on the visible cross-section, σ_{vis}, defined as the product of the BSM production cross-section, the acceptance and the selection efficiency of a BSM signal. When calculating the model-independent upper limits of the A-type regions only the inclusive SRA region is used. Table 7 summarizes the observed (S_{obs}^{95}) and expected (S_{exp}^{95}) 95% CL upper limits on the number of BSM events and on σ_{vis} for all channels and signal

Table 6: Background-only fit results for the A- and B-type regions (top table) and C-type regions (bottom table) performed using 139 fb^{-1} of data. The post-fit uncertainty shows the total statistical + systematic uncertainty.

	SRA	SRA-L	SRA-M	SRA-H	SRB
Observed events	17	12	3	2	3
Fitted SM bkg events	17.1 ± 2.8	8.4 ± 1.7	5.7 ± 0.8	3.0 ± 1.5	3.3 ± 0.9
$t\bar{t}$	10.1 ± 2.5	4.7 ± 1.5	3.7 ± 0.6	1.7 ± 1.4	2.3 ± 0.8
Z+jets	2.6 ± 0.43	1.3 ± 0.2	0.9 ± 0.2	0.4 ± 0.1	0.3 ± 0.06
Single-top	1.4 ± 0.28	0.4 ± 0.1	0.3 ± 0.1	0.6 ± 0.2	0.5 ± 0.1
$t\bar{t}$ +W/Z	1.2 ± 0.26	0.7 ± 0.1	0.3 ± 0.1	0.1 ± 0.0	0.07 ± 0.02
$t\bar{t}$ +h	1.1 ± 0.18	0.7 ± 0.1	0.3 ± 0.1	0.1 ± 0.0	0.13 ± 0.02
W+jets	0.4 ± 0.12	0.2 ± 0.1	0.1 ± 0.0	–	0.02 ± 0.01
Diboson	0.4 ± 0.06	0.3 ± 0.1	–	–	–
$m(\tilde{b}_1, \tilde{\chi}_2^0, \tilde{\chi}_1^0) = (1100, 330, 200)$ GeV	13.7 ± 0.3	0.7 ± 0.1	6.3 ± 0.2	6.6 ± 0.2	0.3 ± 0.1
$m(\tilde{b}_1, \tilde{\chi}_2^0, \tilde{\chi}_1^0) = (700, 680, 550)$ GeV	1.3 ± 0.6	0.2 ± 0.1	0.5 ± 0.4	0.6 ± 0.4	7.4 ± 1.2
$m(\tilde{b}_1, \tilde{\chi}_2^0, \tilde{\chi}_1^0) = (1200, 1150, 60)$ GeV	8.7 ± 0.2	1.4 ± 0.1	3.4 ± 0.1	3.8 ± 0.1	0.6 ± 0.1

	SRC	SRC22	SRC24	SRC26	SRC28
Observed events	47	28	12	4	3
Fitted SM bkg events	37.9 ± 6.2	21.2 ± 4.1	10.6 ± 2.3	3.7 ± 0.9	2.4 ± 0.6
$t\bar{t}$	5.4 ± 2.6	3.9 ± 2.3	1.1 ± 0.6	0.3 ± 0.3	0.1 ± 0.1
Z+jets	17.6 ± 4.7	8.8 ± 2.5	6.0 ± 1.8	1.7 ± 0.7	1.1 ± 0.4
Single-top	5.0 ± 1.5	2.7 ± 1.0	1.2 ± 0.3	0.7 ± 0.2	0.4 ± 0.1
$t\bar{t}$ +W/Z	4.3 ± 0.57	2.5 ± 0.4	1.1 ± 0.2	0.5 ± 0.1	0.2 ± 0.1
$t\bar{t}$ +h	0.2 ± 0.03	0.2 ± 0.0	$0.0^{+0.0}_{-0.0}$	0.1 ± 0.0	0.0 ± 0.0
W+jets	3.5 ± 0.76	2.2 ± 0.5	0.6 ± 0.2	0.2 ± 0.1	0.4 ± 0.1
Diboson	1.8 ± 0.32	0.9 ± 0.2	0.6 ± 0.1	0.2 ± 0.0	0.1 ± 0.1
$m(\tilde{b}_1, \tilde{\chi}_2^0, \tilde{\chi}_1^0) = (1100, 330, 200)$ GeV	0.4 ± 0.06	0.3 ± 0.05	0.1 ± 0.03	0.03 ± 0.02	0.03 ± 0.01
$m(\tilde{b}_1, \tilde{\chi}_2^0, \tilde{\chi}_1^0) = (700, 680, 550)$ GeV	1.2 ± 0.5	0.5 ± 0.2	0.7 ± 0.4	–	–
$m(\tilde{b}_1, \tilde{\chi}_2^0, \tilde{\chi}_1^0) = (1200, 1150, 60)$ GeV	26.7 ± 0.3	6.3 ± 0.2	6.4 ± 0.2	5.8 ± 0.2	8.3 ± 0.2

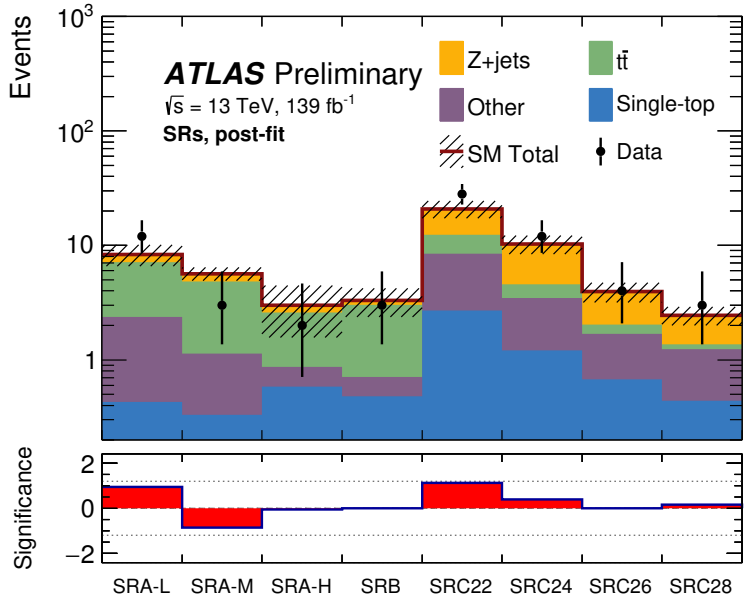

Figure 6: Results of the background-only fit extrapolated to all SRs. The normalisation of the backgrounds is obtained from the fit to the CRs. The upper panel shows the observed number of events and the predicted background yields. The backgrounds which contribute only a small amount (diboson, W+jets and $t\bar{t}+W/Z/h$) are grouped and labelled as "Other". All uncertainties defined in Section 7 are included in the uncertainty band. The lower panel shows the significance in each SR. The significance calculation is performed as described in Ref. [82].

regions. The p_0-values, which represent the probability of the SM background to fluctuate to the observed number of events or higher, are also provided and are capped at $p_0 = 0.5$; the associated significance is provided in parentheses.

Table 7: From left to right, observed 95% CL upper limits on the visible cross sections σ_{vis}, the observed (S^{95}_{obs}) and expected (S^{95}_{exp}) 95% CL upper limits on the number of signal events with ± 1 σ excursions of the expectation, the CL of the background-only hypothesis, CL_B, the discovery p-value (p_0), truncated at 0.5, and the associated significance (in parentheses).

Signal channel	σ_{vis}[fb]	S^{95}_{obs}	S^{95}_{exp}	CL_B	p_0 (Z)
SRA	0.06	9.0	$10.1^{+4.7}_{-3.1}$	0.38	0.50 (0.00)
SRB	0.04	4.9	$5.1^{+2.8}_{-1.7}$	0.45	0.50 (0.00)
SRC	0.19	26.0	$20.8^{+7.0}_{-5.5}$	0.80	0.17 (0.97)

Model-dependent exclusion limits are obtained assuming the two types of SUSY particle mass hierarchies described in Section 1. The lightest bottom-squark decays exclusively via $\tilde{b}_1 \rightarrow b\tilde{\chi}^0_2$ with subsequent decay $\tilde{\chi}^0_2 \rightarrow h\tilde{\chi}^0_1$. The expected limits from the SRs are compared for each set of scenarios and the observed limits are obtained by choosing the SR with the best expected sensitivity for each SUSY model. The fit procedure takes into account correlations in the yield predictions between control and signal regions due to common background normalisation parameters and systematic uncertainties. The experimental

systematic uncertainties in the signal are taken into account for the calculation and are assumed to be fully correlated with those in the SM background.

Figures 8(a) and 8(b) show the observed (solid line) and expected (dashed line) exclusion contours at 95% CL in the $\tilde{b}_1$–$\tilde{\chi}_2^0$ mass planes for the two types of SUSY scenarios considered. For the scenarios where the mass of the neutralino is assumed to be 60 GeV, the sensitivity to models with the largest mass difference between the $\tilde{b}_1$ and the $\tilde{\chi}_2^0$ is achieved with the combination of the A-type SRs. Sensitivity to scenarios with small mass differences is obtained with the dedicated C-type SRs. For scenarios with $\Delta m(\tilde{\chi}_2^0, \tilde{\chi}_1^0) = 130$ GeV, the sensitivity of the A-type SRs is complemented by the B-type SR in the case of small mass difference between the $\tilde{b}_1$ and the $\tilde{\chi}_2^0$.

Bottom-squark masses up to 1.45 TeV are excluded for models with fixed $m_{\tilde{\chi}_1^0} = 60$ GeV and $\tilde{\chi}_2^0$ masses between 500 GeV and 1.1 TeV. In case of $\Delta m(\tilde{\chi}_2^0, \tilde{\chi}_1^0) = 130$ GeV, bottom-squark masses up to 1.2 TeV are excluded for $\tilde{\chi}_2^0$ masses up to 750 GeV. The loss in sensitivity for models where $\tilde{\chi}_2^0$ masses are below 190 GeV is due to the stringent requirements on $E_{\mathrm{T}}^{\mathrm{miss}}$.

The results constitute a large improvement upon previous Run-1 searches and significantly strengthen the constraints on bottom-squark masses, being also complementary to other searches where bottom-squarks are assumed to decay directly to $\tilde{\chi}_1^0$ and one b-quark or to top quarks and charginos [87].

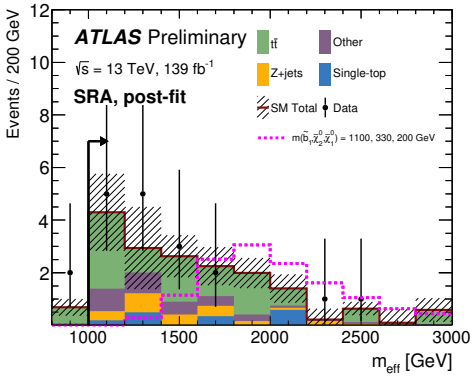

(a) SRA m_{eff}

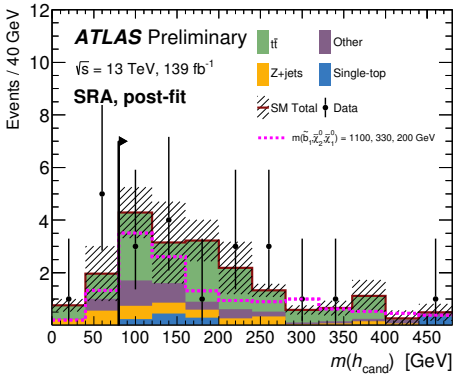

(b) SRA $m(h_{\text{cand}})$

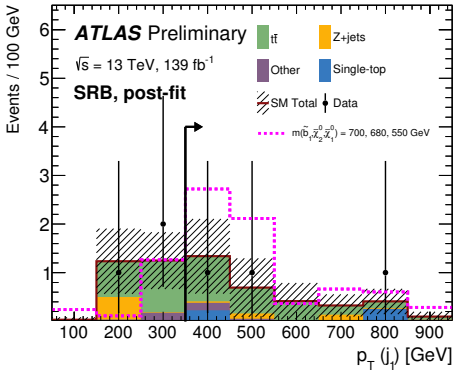

(c) SRB p_{T} (j_1)

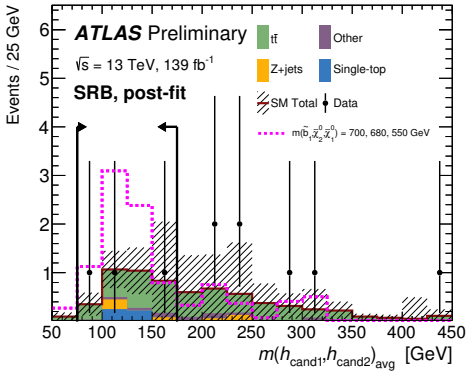

(d) SRB $m(h_{\text{cand1}}, h_{\text{cand2}})_{\text{avg}}$

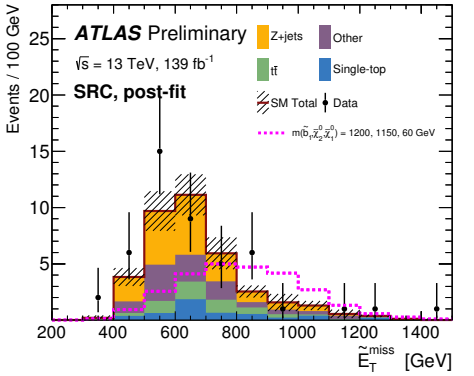

(e) SRC $E_{\text{T}}^{\text{miss}}$

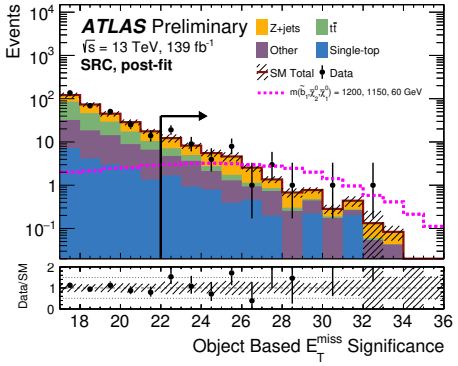

(f) SRC $\mathcal{S}$

Figure 7: Post-fit distributions of (a) the m_{eff} and (b) the $m(h_{\text{cand}})$ in the inclusive SRA region; (c) the leading jet p_{T} and (d) the $m(h_{\text{cand1}}, h_{\text{cand2}})_{\text{avg}}$ for the average mass of the Higgs candidates in the SRB region; (e) $E_{\text{T}}^{\text{miss}}$ and (f) $\mathcal{S}$ for SRC regions. All SR selections are applied except for the selection on the variable shown, where the selection on the variable under consideration is denoted by an arrow, except in the case of (e), where the full SRC selection is applied. All uncertainties as defined in Section 7 are included in the uncertainty band. The backgrounds which contribute only a small amount (diboson, W+jets and $t\bar{t}$ +$W/Z/h$) are grouped and labelled as "Other". For illustration, contributions expected for scenarios with different bottom-squark, $\tilde{\chi}_2^0$ and $\tilde{\chi}_1^0$ masses depending on the SR considered are superimposed. Overflow events which do not fall into the axis range are placed into the right-most bin.

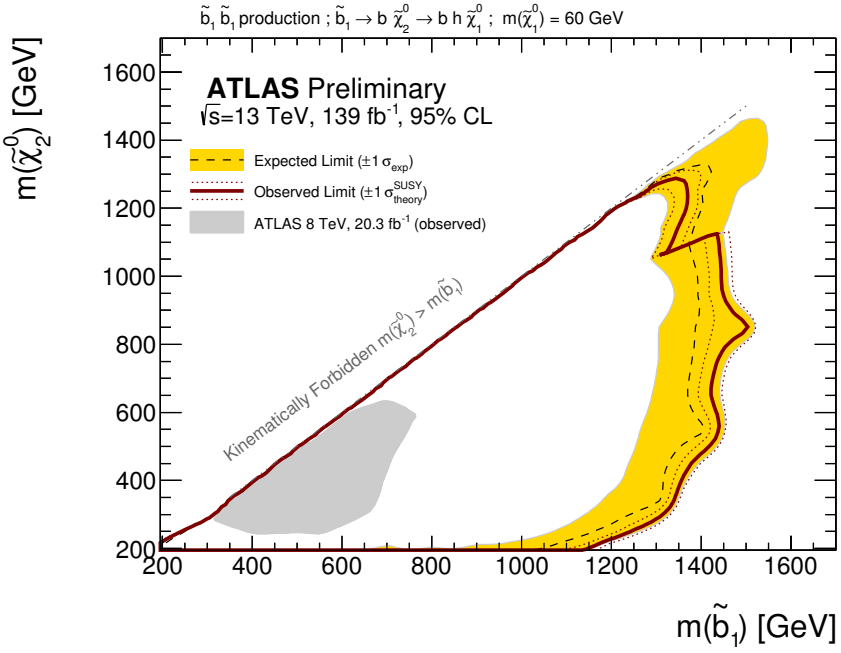

(a) $m(\tilde{\chi}_1^0) = 60\,\text{GeV}$ signal scenario.

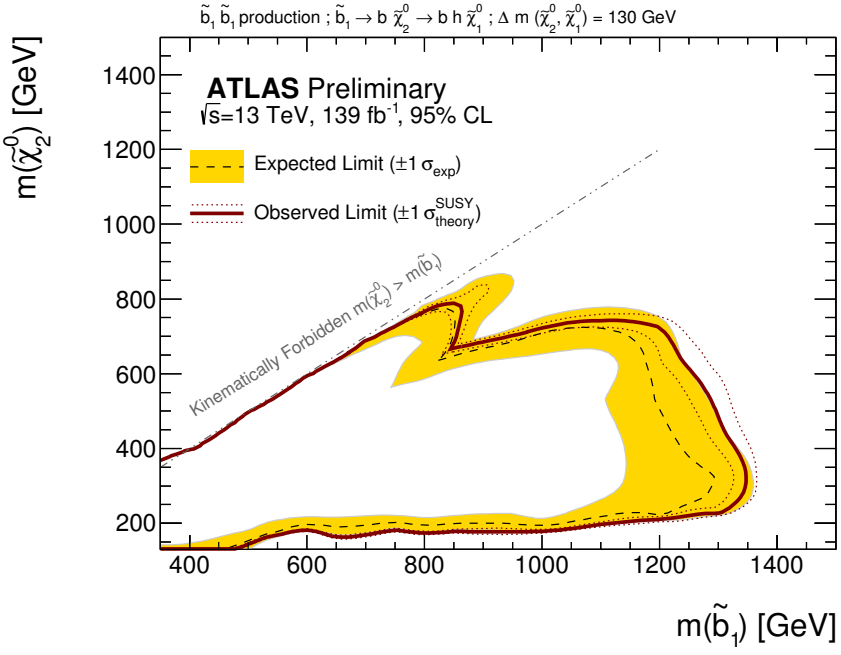

(b) $\Delta m(\tilde{\chi}_2^0, \tilde{\chi}_1^0) = 130\,\text{GeV}$ signal scenario.

Figure 8: Exclusion contour at the 95% CL in the $m(\tilde{b}_1, \tilde{\chi}_2^0)$ phase space for (a) the $m(\tilde{\chi}_1^0) = 60\,\text{GeV}$ signal scenario, ATLAS Run 1 limit taken from Ref. [21] and (b) the $\Delta m(\tilde{\chi}_2^0, \tilde{\chi}_1^0) = 130\,\text{GeV}$ signal scenario, using the SR with the best-expected sensitivity. The theory uncertainty band contains the systematic uncertainties on the signal model under consideration and the uncertainty in the signal cross section.

9 Conclusion

The result of a search for pair production of bottom-squarks is reported. The analysis uses 139 fb^{-1} of pp collisions at $\sqrt{s}$ = 13 TeV collected by the ATLAS experiment at the LHC between 2015 and 2018. R-parity conserving SUSY scenarios where bottom-squarks decay to a b-quark and the second lightest neutralino, $\tilde{b}_1 \rightarrow b + \tilde{\chi}_2^0$, with $\tilde{\chi}_2^0$ subsequently decaying to a SM-like Higgs boson and the lightest neutralino, are considered. The search investigates final states containing large missing transverse momentum and three or more b-jets. No significant excess of events above the expected Standard Model background is found and exclusion limits at the 95% confidence level are placed on both the visible cross-section, and on the mass of the bottom-squark under various assumptions on the mass hierarchy of the $\tilde{b}_1$, $\tilde{\chi}_2^0$ and $\tilde{\chi}_1^0$. Bottom-squark masses up to 1.45 (1.2) TeV are excluded for $\tilde{\chi}_2^0$ masses up to 1100 (750) GeV in models with fixed $m(\tilde{\chi}_1^0)$ = 60 GeV ($\Delta m(\tilde{\chi}_2^0, \tilde{\chi}_1^0)$ = 130 GeV). As the first search for such scenarios carried out by ATLAS in Run 2, these results are a significant improvement upon the previous Run-1 result and considerably further the constraints on bottom-squark production.

References

[1] Yu. A. Golfand and E. P. Likhtman, *Extension of the Algebra of Poincare Group Generators and Violation of p Invariance*, JETP Lett. **13** (1971) 323–326, [Pisma Zh. Eksp. Teor. Fiz. **13**, 452 (1971)].

[2] D. V. Volkov and V. P. Akulov, *Is the Neutrino a Goldstone Particle?*, Phys. Lett. B **46** (1973) 109–110.

[3] J. Wess and B. Zumino, *Supergauge Transformations in Four-Dimensions*, Nucl. Phys. B **70** (1974) 39–50.

[4] J. Wess and B. Zumino, *Supergauge Invariant Extension of Quantum Electrodynamics*, Nucl. Phys. B **78** (1974) 1.

[5] S. Ferrara and B. Zumino, *Supergauge Invariant Yang-Mills Theories*, Nucl. Phys. B **79** (1974) 413.

[6] A. Salam and J. A. Strathdee, *Supersymmetry and Nonabelian Gauges*, Phys. Lett. B **51** (1974) 353–355.

[7] N. Sakai, *Naturalness in Supersymmetric Guts*, Z. Phys. C **11** (1981) 153.

[8] S. Dimopoulos, S. Raby, and F. Wilczek, *Supersymmetry and the Scale of Unification*, Phys. Rev. D **24** (1981) 1681–1683.

[9] L. E. Ibanez and G. G. Ross, *Low-Energy Predictions in Supersymmetric Grand Unified Theories*, Phys. Lett. B **105** (1981) 439.

[10] S. Dimopoulos and H. Georgi, *Softly Broken Supersymmetry and SU(5)*, Nucl. Phys. B **193** (1981) 150.

[11] G. R. Farrar and P. Fayet, *Phenomenology of the Production, Decay, and Detection of New Hadronic States Associated with Supersymmetry*, Phys. Lett. B **76** (1978) 575–579.

[12] H. Goldberg, *Constraint on the Photino Mass from Cosmology*, Phys. Rev. Lett. **50** (1983) 1419, [Erratum: Phys. Rev. Lett. **103**, 099905 (2009)].

[13] J. R. Ellis, J. S. Hagelin, D. V. Nanopoulos, K. A. Olive, and M. Srednicki, *Supersymmetric Relics from the Big Bang*, Nucl. Phys. B **238** (1984) 453–476.

[14] R. Barbieri and G. F. Giudice, *Upper Bounds on Supersymmetric Particle Masses*, Nucl. Phys. B **306** (1988) 63.

[15] B. de Carlos and J. A. Casas, *One loop analysis of the electroweak breaking in supersymmetric models and the fine tuning problem*, Phys. Lett. B **309** (1993) 320–328, arXiv:hep-ph/9303291 [hep-ph].

[16] P. Fayet, *Supersymmetry and Weak, Electromagnetic and Strong Interactions*, Phys. Lett. B **64** (1976) 159.

[17] P. Fayet, *Spontaneously Broken Supersymmetric Theories of Weak, Electromagnetic and Strong Interactions*, Phys. Lett. B **69** (1977) 489.

[18] ATLAS Collaboration, *Observation of $H \to b\bar{b}$ decays and VH production with the ATLAS detector*, Phys. Lett. B **786** (2018) 59, arXiv:1808.08238 [hep-ex].

[19] J. Alwall, M.-P. Le, M. Lisanti, and J. G. Wacker, *Searching for Directly Decaying Gluinos at the Tevatron*, Phys. Lett. B **666** (2008) 34, arXiv:0803.0019 [hep-ph].

[20] J. Alwall, P. Schuster, and N. Toro, *Simplified Models for a First Characterization of New Physics at the LHC*, Phys. Rev. D **79** (2009) 075020, arXiv:0810.3921 [hep-ph].

[21] ATLAS Collaboration, *ATLAS Run 1 searches for direct pair production of third-generation squarks at the Large Hadron Collider*, Eur. Phys. J. C **75** (2015) 510, arXiv:1506.08616 [hep-ex], [Erratum: Eur. Phys. J. C **76**, 153 (2016)].

[22] M. Escudero, A. Berlin, D. Hooper, and M.-X. Lin, *Toward (Finally!) Ruling Out Z and Higgs Mediated Dark Matter Models*, JCAP **1612** (2016) 029, arXiv:1609.09079 [hep-ph].

[23] CMS Collaboration, *Search for supersymmetry with Higgs boson to diphoton decays using the razor variables at* $\sqrt{s}$ *= 13 TeV*, Phys. Lett. B **779** (2018) 166–190, arXiv:1709.00384 [hep-ex].

[24] ATLAS Collaboration, *The ATLAS Experiment at the CERN Large Hadron Collider*, JINST **3** (2008) S08003.

[25] ATLAS Collaboration, *ATLAS Insertable B-Layer Technical Design Report*, ATLAS-TDR-19, 2010, http://cds.cern.ch/record/1291633, Addendum: ATLAS-TDR-19-ADD-1, 2012, http://cds.cern.ch/record/1451888.

[26] ATLAS Collaboration, *Performance of the ATLAS Trigger System in 2015*, Eur. Phys. J. C **77** (2017) 317, arXiv:1611.09661 [hep-ex].

[27] ATLAS Collaboration, *Luminosity determination in pp collisions at* $\sqrt{s}$ *= 8 TeV using the ATLAS detector at the LHC*, Eur. Phys. J. C **76** (2016) 653, arXiv:1608.03953 [hep-ex].

[28] G. Avoni et al., *The new LUCID-2 detector for luminosity measurement and monitoring in ATLAS*, JINST **13** (2018) P07017.

[29] ATLAS Collaboration, *2015 start-up trigger menu and initial performance assessment of the ATLAS trigger using Run-2 data*, ATL-DAQ-PUB-2016-001, 2016, https://cds.cern.ch/record/2136007.

[30] ATLAS Collaboration, *The ATLAS Simulation Infrastructure*, Eur. Phys. J. C **70** (2010) 823, arXiv:1005.4568 [physics.ins-det].

[31] S. Agostinelli et al., *GEANT4: A simulation toolkit*, Nucl. Instrum. Meth. A **506** (2003) 250.

[32] J. Alwall et al., *The automated computation of tree-level and next-to-leading order differential cross sections, and their matching to parton shower simulations*, JHEP **07** (2014) 079, arXiv:1405.0301 [hep-ph].

[33] T. Sjöstrand, S. Ask, J. R. Christiansen, R. Corke, N. Desai, P. Ilten, S. Mrenna, S. Prestel, C. O. Rasmussen, and P. Z. Skands, *An Introduction to PYTHIA 8.2*, Comput. Phys. Commun. **191** (2015) 159, arXiv:1410.3012 [hep-ph].

[34] ATLAS Collaboration, *ATLAS Pythia 8 tunes to 7 TeV data*, ATL-PHYS-PUB-2014-021, 2014, https://cds.cern.ch/record/1966419.

[35] L. Lönnblad and S. Prestel, *Merging Multi-leg NLO Matrix Elements with Parton Showers*, JHEP **03** (2013) 166, arXiv:1211.7278 [hep-ph].

[36] R. D. Ball et al., *Parton distributions with LHC data*, Nucl. Phys. B **867** (2013) 244, arXiv:1207.1303 [hep-ph].

[37] W. Beenakker, C. Borschensky, M. Krämer, A. Kulesza, and E. Laenen, *NNLL-fast: predictions for coloured supersymmetric particle production at the LHC with threshold and Coulomb resummation*, JHEP **12** (2016) 133, arXiv:1607.07741 [hep-ph].

[38] W. Beenakker, R. Hopker, M. Spira, and P. Zerwas, *Squark and gluino production at hadron colliders*, Nucl. Phys. B **492** (1997) 51–103, arXiv:hep-ph/9610490 [hep-ph].

[39] W. Beenakker, S. Brensing, M. Kramer, A. Kulesza, E. Laenen, and I. Niessen, *Supersymmetric top and bottom squark production at hadron colliders*, JHEP **08** (2010) 098, arXiv:1006.4771 [hep-ph].

[40] W. Beenakker, C. Borschensky, R. Heger, M. Krämer, A. Kulesza, and E. Laenen, *NNLL resummation for stop pair-production at the LHC*, JHEP **05** (2016) 153, arXiv:1601.02954 [hep-ph].

[41] J. Butterworth et al., *PDF4LHC recommendations for LHC Run II*, J. Phys. G **43** (2016) 023001, arXiv:1510.03865 [hep-ph].

[42] S. Alioli, P. Nason, C. Oleari, and E. Re, *A general framework for implementing NLO calculations in shower Monte Carlo programs: the POWHEG BOX*, JHEP **06** (2010) 043, arXiv:1002.2581 [hep-ph].

[43] ATLAS Collaboration, *Further studies on simulation of top-quark production for the ATLAS experiment at* $\sqrt{s}$ = 13 *TeV*, ATL-PHYS-PUB-2016-016, 2016, https://cds.cern.ch/record/2205262.

[44] T. Gleisberg et al., *Event generation with SHERPA 1.1*, JHEP **02** (2009) 007, arXiv:0811.4622 [hep-ph].

[45] T. Gleisberg and S. Höche, *Comix, a new matrix element generator*, JHEP **12** (2008) 039, arXiv:0808.3674 [hep-ph].

[46] F. Cascioli, P. Maierhofer, and S. Pozzorini, *Scattering Amplitudes with Open Loops*, Phys. Rev. Lett. **108** (2012) 111601, arXiv:1111.5206 [hep-ph].

[47] S. Schumann and F. Krauss, *A Parton shower algorithm based on Catani-Seymour dipole factorisation*, JHEP **03** (2008) 038, arXiv:0709.1027 [hep-ph].

[48] S. Höche, F. Krauss, M. Schönherr, and F. Siegert, *QCD matrix elements + parton showers: The NLO case*, JHEP **04** (2013) 027, arXiv:1207.5030 [hep-ph].

[49] ATLAS Collaboration, *Search for squarks and gluinos with the ATLAS detector in final states with jets and missing transverse momentum using 4.7* fb^{-1} *of* $\sqrt{s}$ = 7 *TeV proton-proton collision data*, Phys. Rev. D **87** (2013) 012008, arXiv:1208.0949 [hep-ex].

[50] M. Beneke, P. Falgari, S. Klein, and C. Schwinn, *Hadronic top-quark pair production with NNLL threshold resummation*, Nucl. Phys. B **855** (2012) 695, arXiv:1109.1536 [hep-ph].

[51] M. Cacciari, M. Czakon, M. Mangano, A. Mitov, and P. Nason, *Top-pair production at hadron colliders with next-to-next-to-leading logarithmic soft-gluon resummation*, Phys. Lett. B **710** (2012) 612, arXiv:1111.5869 [hep-ph].

[52] P. Bärnreuther, M. Czakon, and A. Mitov, *Percent Level Precision Physics at the Tevatron: First Genuine NNLO QCD Corrections to $q\bar{q} \to t\bar{t} + X$*, Phys. Rev. Lett. **109** (2012) 132001, arXiv:1204.5201 [hep-ph].

[53] M. Czakon and A. Mitov, *NNLO corrections to top-pair production at hadron colliders: the all-fermionic scattering channels*, JHEP **12** (2012) 054, arXiv:1207.0236 [hep-ph].

[54] M. Czakon and A. Mitov, *NNLO corrections to top pair production at hadron colliders: the quark-gluon reaction*, JHEP **01** (2013) 080, arXiv:1210.6832 [hep-ph].

[55] M. Czakon, P. Fiedler, and A. Mitov, *Total Top-Quark Pair-Production Cross Section at Hadron Colliders Through $O(\alpha_S^4)$*, Phys. Rev. Lett. **110** (2013) 252004, arXiv:1303.6254 [hep-ph].

[56] M. Czakon and A. Mitov, *Top++: A Program for the Calculation of the Top-Pair Cross-Section at Hadron Colliders*, Comput. Phys. Commun. **185** (2014) 2930, arXiv:1112.5675 [hep-ph].

[57] N. Kidonakis, *Next-to-next-to-leading-order collinear and soft gluon corrections for t-channel single top quark production*, Phys. Rev. D **83** (2011) 091503, arXiv:1103.2792 [hep-ph].

[58] N. Kidonakis, *NNLL resummation for s-channel single top quark production*, Phys. Rev. D **81** (2010) 054028, arXiv:1001.5034 [hep-ph].

[59] N. Kidonakis, *Two-loop soft anomalous dimensions for single top quark associated production with a W- or H-*, Phys. Rev. D **82** (2010) 054018, arXiv:1005.4451 [hep-ph].

[60] D. J. Lange, *The EvtGen particle decay simulation package*, Nucl. Instrum. Meth. A **462** (2001) 152.

[61] ATLAS Collaboration, *Summary of ATLAS Pythia 8 tunes*, ATL-PHYS-PUB-2012-003, 2012, https://cds.cern.ch/record/1474107.

[62] A. D. Martin, W. J. Stirling, R. S. Thorne, and G. Watt, *Parton distributions for the LHC*, Eur. Phys. J. C **63** (2009) 189–285, arXiv:0901.0002 [hep-ph].

[63] ATLAS Collaboration, *Vertex Reconstruction Performance of the ATLAS Detector at $\sqrt{s} = 13$ TeV*, ATL-PHYS-PUB-2015-026, 2015, https://cds.cern.ch/record/2037717.

[64] ATLAS Collaboration, *Topological cell clustering in the ATLAS calorimeters and its performance in LHC Run 1*, Eur. Phys. J. C **77** (2016) 490, arXiv:1603.02934 [hep-ex].

[65] M. Cacciari, G. P. Salam, and G. Soyez, *The Anti-k(t) jet clustering algorithm*, JHEP **04** (2008) 063, arXiv:0802.1189 [hep-ph].

[66] M. Cacciari, G. P. Salam, and G. Soyez, *FastJet User Manual*, Eur. Phys. J. C **72** (2012) 1896, arXiv:1111.6097 [hep-ph].

[67] ATLAS Collaboration, *Jet energy scale measurements and their systematic uncertainties in proton–proton collisions at $\sqrt{s} = 13$ TeV with the ATLAS detector*, Phys. Rev. D **96** (2017) 072002, arXiv:1703.09665 [hep-ex].

[68] ATLAS Collaboration, *Selection of jets produced in 13 TeV proton-proton collisions with the ATLAS detector*, ATLAS-CONF-2015-029. https://cds.cern.ch/record/2037702.

[69] ATLAS Collaboration, *Constituent-level pile-up mitigation techniques in ATLAS*, ATLAS-CONF-2017-065. https://cds.cern.ch/record/2281055.

[70] ATLAS Collaboration, *Measurements of b-jet tagging efficiency with the ATLAS detector using $t\bar{t}$ events at $\sqrt{s}$ = 13 TeV*, JHEP **08** (2018) 089, arXiv:1805.01845 [hep-ex].

[71] ATLAS Collaboration, *Electron reconstruction and identification in the ATLAS experiment using the 2015 and 2016 LHC proton-proton collision data at $\sqrt{s}$ = 13 TeV*, Submitted to: Eur. Phys. J. C (2019), arXiv:1902.04655 [physics.ins-det].

[72] ATLAS Collaboration, *Electron and photon energy calibration with the ATLAS detector using 2015-2016 LHC proton-proton collision data*, JINST **14** (2019) P03017, arXiv:1812.03848 [hep-ex].

[73] ATLAS Collaboration, *Muon reconstruction performance of the ATLAS detector in proton–proton collision data at $\sqrt{s}$ = 13 TeV*, Eur. Phys. J. C **76** (2016) 292, arXiv:1603.05598 [hep-ex].

[74] ATLAS Collaboration, *Measurement of the $t\bar{t}$ production cross-section using $e\mu$ events with b-tagged jets in pp collisions at $\sqrt{s}$ = 13 TeV with the ATLAS detector*, Phys. Lett. B **761** (2016) 136, arXiv:1606.02699 [hep-ex].

[75] ATLAS Collaboration, *Measurement of the photon identification efficiencies with the ATLAS detector using LHC Run 2 data collected in 2015 and 2016*, Eur. Phys. J. C **79** (2019) 205, arXiv:1810.05087 [hep-ex].

[76] ATLAS Collaboration, *E_T^{miss} performance in the ATLAS detector using 2015-2016 LHC p-p collisions*, ATLAS-CONF-2018-023. http://cds.cern.ch/record/2625233.

[77] ATLAS Collaboration, *Performance of algorithms that reconstruct missing transverse momentum in $\sqrt{s}$ = 8 TeV proton–proton collisions in the ATLAS detector*, Eur. Phys. J. C **77** (2017) 241, arXiv:1609.09324 [hep-ex].

[78] ATLAS Collaboration, *Jet energy measurement with the ATLAS detector in proton–proton collisions at $\sqrt{s}$ = 7 TeV*, Eur. Phys. J. C **73** (2013) 2304, arXiv:1112.6426 [hep-ex].

[79] I. Hinchliffe, F. E. Paige, M. D. Shapiro, J. Soderqvist, and W. Yao, *Precision SUSY measurements at CERN LHC*, Phys. Rev. D **55** (1997) 5520–5540, arXiv:hep-ph/9610544 [hep-ph].

[80] ATLAS Collaboration, *Object-based missing transverse momentum significance in the ATLAS detector*, ATLAS-CONF-2018-038. http://cds.cern.ch/record/2630948.

[81] M. Baak et al., *HistFitter software framework for statistical data analysis*, Eur. Phys. J. C **75** (2015) 153, arXiv:1410.1280 [hep-ex].

[82] G. Choudalakis and D. Casadei, *Plotting the differences between data and expectation*, European Physical Journal Plus **127** (2012) 25, arXiv:1111.2062 [physics.data-an].

[83] ATLAS Collaboration, *Jet energy resolution in proton–proton collisions at $\sqrt{s}$ = 7 TeV recorded in 2010 with the ATLAS detector*, Eur. Phys. J. C **73** (2013) 2306, arXiv:1210.6210 [hep-ex].

[84] M. Bähr et al., *Herwig++ Physics and Manual*, Eur. Phys. J. C **58** (2008) 639, arXiv:0803.0883.

[85] J. Bellm et al., *Herwig 7.0/Herwig++ 3.0 release note*, Eur. Phys. J. C **76** (2016) 196, arXiv:1512.01178 [hep-ph].

[86] A. L. Read, *Presentation of search results: The CL(s) technique*, J. Phys. G **28** (2002) 2693.

[87] ATLAS Collaboration, *Search for supersymmetry in events with b-tagged jets and missing transverse momentum in pp collisions at* $\sqrt{s}$ = 13 *TeV with the ATLAS detector*, JHEP **11** (2017) 195, arXiv:1708.09266 [hep-ex].